DEPARTAMENT OF MATERIALS SCIENCE

MARIA MEIRELES RIBEIRO MAGALHÃES

BSc in Micro and Nanotechnology Engineering

OPTIMIZATION OF RF MAGNETRON SPUTTERING OF CERIUM-DOPED INDIUM OXIDE FOR SILICON HETEROJUNCTION SOLAR CELLS

MASTER IN MICRO AND NANOTECHNOLOGY ENGINEERING

NOVA University Lisbon
September, 2023

DEPARTAMENT OF MATERIALS SCIENCE

OPTIMIZATION OF RF MAGNETRON SPUTTERING OF CERIUM-DOPED INDIUM OXIDE FOR SILICON HETEROJUNCTION SOLAR CELLS

MARIA MEIRELES RIBEIRO MAGALHÃES

BSc in Micro and Nanotechnology Engineering

Adviser: Prof. dr. Olindo Isabella
Full professor, Delft University of Technology

Co-advisers: Prof. Manuel J. Mendes
Assistant Professor, NOVA School of Science and Technology | FCT NOVA

Examination Committee:

Chair: Prof. Rui Igreja,
Associate Professor, NOVA School of Science and Technology | FCT NOVA

Rapporteurs: Dr. Engin Özkol,
Researcher, Delft University of Technology

Adviser: Prof. Dr. Olindo Isabella,
Full Professor, Delft University of Technology

Members: Prof. Manuel J. Mendes
Assistant Professor, NOVA School of Science and Technology | FCT NOVA

MASTER IN MICRO AND NANOTECHNOLOGY ENGINEERING

NOVA University Lisbon
September, 2023

Optimization of RF Magnetron Sputtering of Cerium-Doped Indium Oxide for Silicon Heterojunction Solar Cells

ACKNOWLEDGMENTS

This five-year journey in the Integrated Master in Micro and Nanotechnology Engineering is now coming to an end. First, I would like to thank the Department of Materials Science, and Professor Rodrigo Martins and Elvira Fortunato for developing my course. To the NOVA School of Science and Technology of the University of Lisbon for being my home during this time, and to Erasmus+ for the opportunity to develop this 6-month thesis abroad. This project was done at the Delft University of Technology, being carried out in the Photovoltaic Materials and Devices (PVMD) group at the faculty of Electrical Engineering, Mathematics and Computer Sciences. It was a wonderful study and work environment, where I got to meet people from all around the world. A big thank you must go to my advisor, Professor Olindo Isabella, for providing me with the opportunity to work on this project within this remarkable group, and for all the assistance and help from the very beginning. I would also like to thank Professor Manuel Mendes, my co-advisor, for his support and guidance in the beginning and as well in the end of my project.

A thanks to my supervisor Yifeng Zhao, for all the assistance in organizing my project and for being available every time I needed. I would also like to thank other PVMD group members: Martijn Tijssen, Stefaan Heirman, Tim Velzeboer and Mehmet Karaman for all the equipment-related assistance, Katarina Kovačević for the incessant help, especially with the PECVD system to fabricate the solar cells used in this work, Liqi Cao for being available to finish fabricating and characterizing the cells even after my project was over, and my colleague Yi for all the help in the cleanroom. To all of you, I wish all the best. I would also like to thank my dear *amigo* Tristan, my first friend in Delft, for welcoming me to the best office in the department, and for all the fun moments we had, and to my amazing friend Shloka, the most heartwarming, hard worker and funny person I have ever met. All the great times that I had in Delft would never have happened without the both of you.

Another thanks goes to all my friends and colleagues that did this five-year journey with me, especially my PGC and BC girlfriends. You are my rock. Thank you for all the joyful crying in these latest months. To all my Praxe family, for teaching me so many valuable things for life, especially to my godchildren Maria and Tiago for choosing me for this so-called parenting role. I hope I was my best version for you. Finally, a big thank you to my boyfriend for sharing this experience abroad with me, for all the support throughout this time, and for always cheering me up even when all seemed to go wrong.

The most important thanks goes to my family for all the endless support, in particular to my parents for helping me have this experience and for always believing in me.

MOTIVATION

This study was motivated by the need to improve the performance of cerium-doped indium oxide (ICO) films as transparent conductive oxide (TCO) in silicon heterojunction solar cells (SHJ-SC). Due to its great efficiency and cost-effectiveness, silicon heterojunction solar cells have grown to be a significant competitor as the worldwide need for clean and sustainable energy solutions grows. The effectiveness of these cells, however, is strongly dependent on the quality of the TCO layers.

While ICO has high electrical conductivity and transparency, the deposition technique has a considerable impact on its attributes. Because suboptimal deposition parameters might result in lower solar cell performance, optimizing the deposition conditions of ICO is a crucial scientific activity. The goal of this research is to maximize the potential of ICO films by precisely tuning the sputtering process. Applying this material to SHJ-SC and increase its efficiency will help in the progress of adopting sustainable energy sources.

ABSTRACT

Optimizing solar cell performance hinges significantly on perfecting the Transparent Conductive Oxide (TCO) layer, a critical component for efficient charge collection and light transmission in the solar cell. Due to their high electron mobilities, TCO materials based on In_2O_3 appear to be particularly interesting options for solar applications. Indium Tin Oxide (ITO) is one of the most well-known and widely used TCO materials, but its performance is hindered by parasitic free carrier absorption and light reflection, particularly in the near-infrared (NIR) spectrum. To overcome these issues, researchers have turned their focus to other doped-indium oxides. This study will focus on optimizing sputtered Cerium-doped Indium Oxide (ICO) for application in Silicon Heterojunction solar cells (SHJ-SC). ICO's wide bandgap, exceeding 3.6 eV, guarantees that a larger fraction of the solar spectrum reaches the silicon absorber layers. Notably, ICO exhibits remarkable electron mobilities, surpassing 130 cm^2/Vs when deposited with a heated substrate. However, due to equipment constraints, all depositions in this study were done at room temperature. To elevate ICO's optoelectrical properties, optimization of deposition parameters, such as oxygen flow, chamber pressure, sputtering power, and water vapor partial pressure, was performed. This optimization yielded films with enhanced mobilities and transparency, outperforming conventional laboratory-standard ITO films.

For a 35-nm-thick ICO layer, we achieved a mobility of 44.22 cm^2/Vs, an average transmittance of 85.23% and a resistivity of 8.56×10^{-4} $\Omega\cdot cm$. With the ICO:H layer, we achieved a mobility of 44.56 cm^2/Vs, an average transmittance of 84.77%, and a resistivity of 7.28×10^{-4} $\Omega\cdot cm$. At the device level, we obtained impressive efficiencies of 23.58% and 23.57% for cells employing ICO and ICO:H, respectively. The former showcased a high V_{oc} of 0.722 V, while the latter achieved a J_{sc} of 40.53 mA/cm^2. These results place ICO as a promising alternative for ITO as TCO in diverse photovoltaic applications.

Keywords: SHJ solar cells, TCO, Cerium-doped Indium Oxide, RF magnetron sputtering

RESUMO

A otimização de uma célula solar depende significativamente do aperfeiçoamento da camada de óxido condutor transparente (TCO), crítico para a coleta eficiente de carga e para a transmissão de luz. Devido às suas elevadas mobilidades, os TCOs baseados em In_2O_3 são opções interessantes para aplicações solares. O óxido de índio e estanho (ITO) é um dos TCOs mais conhecidos e utilizados, mas o seu desempenho é prejudicado pela absorção de transportadores livres parasitas e pela reflexão da luz, particularmente no infravermelho próximo (NIR). Para superar esses problemas, o foco está a virar-se para outros óxidos de índio dopados. Este projeto concentra-se na otimização de óxido de índio dopado com cério (ICO) para aplicação em células solares de heterojunção de silício (SHJ). A ampla *bandgap* do ICO, superior a 3.6 eV, garante que uma maior fração do espectro solar atinja as camadas absorventes da célula. O ICO exibe mobilidades elevadas, ultrapassando 130 cm^2/Vs quando depositado num substrato aquecido. No entanto, devido a restrições de equipamento, todas as deposições neste estudo foram feitas à temperatura ambiente. Para elevar as propriedades optoelétricas do ICO, foi realizada a otimização de alguns parâmetros de deposição, como fluxo de oxigênio, pressão na câmara, potência de pulverização, e pressão parcial de vapor de água. Esta otimização levou a filmes com elevadas mobilidade e transparência, superando os filmes de ITO convencionais.

Para uma camada de 35 nm de espessura, o ICO alcançou mobilidade de 44.22 cm^2/Vs, transmitância média de 85.23%, e resistividade de 8.56×10^{-4} Ω·cm. O ICO:H alcançou mobilidade de 44.56 cm^2/Vs, transmitância média de 84.77%, e resistividade de 7.28×10^{-4} Ω·cm. No dispositivo final, obtivemos eficiências de 23.58% e 23.57% para células com ICO e ICO:H, respetivamente. A primeira apresentou um alto V_{oc} de 0.722 V, enquanto a última alcançou um alto J_{sc} de 40.53 mA/cm^2. Estes resultados colocam o ICO como uma alternativa promissora para ITO como TCO em diversas aplicações fotovoltaicas.

Palavras chave: Células solares de SHJ, TCO, Óxido de Índio dopado com Cério, Pulverização

CONTENTS

LIST OF FIGURES

LIST OF TABLES

1

INTRODUCTION

1.1 Solar Photovoltaics Demand

Solar Photovoltaics (PV) emerges as a crucial catalyst in the landscape of global clean energy transformations. Its importance is rooted in its capacity to serve as a fundamental driver in achieving worldwide energy and climate ambitions. This need for renewable energy transition comes from multifaceted causes, with climate change and global warming at the forefront, stemming from the unsustainable use of non-renewable energy sources like oil, coal, and natural gas, which contribute to harmful greenhouse gas emissions[1]. Also, the continuous increase of the world's population, coupled with the ever-rising energy requisites, contribute to this demand for change. In response to these challenges, the global energy sector is embracing the Net Zero Emissions Scenario (NZE)[2], which outlines a roadmap to reach a state where the net amount of CO_2 emissions produced is reduced to zero (the amount of greenhouse gas we produce is no more than the amount taken away). To meet these ambitions, it is required for the solar PV to remarkably upscale manufacturing capacity.

According to a study by the International Energy Agency (IEA)[3], from 1990 to 2019 there was a remarkable expansion rate for solar PV and wind power. These renewables experienced impressive average annual growth rates of 36.0% and 22.6%, respectively, during this period. A significant milestone in 2022 saw solar PV power generation surge by a record-breaking 270 TWh, constituting a 26% surge from the preceding year. This positioned solar PV as accountable for 4.5% of the total global electricity generation, being the third-largest contributor among renewable electricity technologies, behind wind and hydropower[4]. Projecting forward to align with the Net Zero Scenario, an ambitious target of approximately 8,300 TWh in annual solar PV power generation by 2030 was set. To bridge the vast gap from the current capacity of 1,300 TWh, an average annual growth rate of around 26% between 2023 and 2030 is required[4]. This growth was witnessed in 2022, yet sustaining this remarkable momentum within the PV market relies on unwavering and enduring efforts.

1.2 Market Share of Different Solar Cell Technologies

There are numerous solar cells' technologies and designs that provide a wide range of solutions for effective solar energy conversion, each with its own set of advantages. Figure 1.1 displays the market shares of different cell technologies worldwide, reported by The International Technology Roadmap for Photovoltaic (ITRPV)[5]. This report shows that there are three main technologies being explored and employed in industry: TOPCon (Tunnel Oxide Passivated Contact), PERC (Passivated Emitter Rear Cell), and SHJ (Silicon Heterojunction) cells. The choice among these technologies' hinges on factors like efficiency needs, compatibility, and cost considerations, collectively shaping the dynamic landscape of solar photovoltaics to meet diverse market demands for sustainable energy solutions.

The leader of market shares[5] is PERC. This cell presents a rear passivation layer, which increases efficiency by lowering recombination losses[6]. In contrast, TOPCon cells are on the ascent due to compatibility with existing manufacturing processes and cost competitiveness. This technology shows impressive efficiency and passivation capability, obtained by applying a tunnel oxide layer to the cell's surface, considerably decreasing recombination losses[7]. SHJ cells are emerging as a promising contender, harnessing the power of multiple semiconductor materials to achieve high efficiency. These cells combine amorphous and crystalline silicon layers, allowing for efficient charge carrier separation and collection, diminishing energy losses[8].

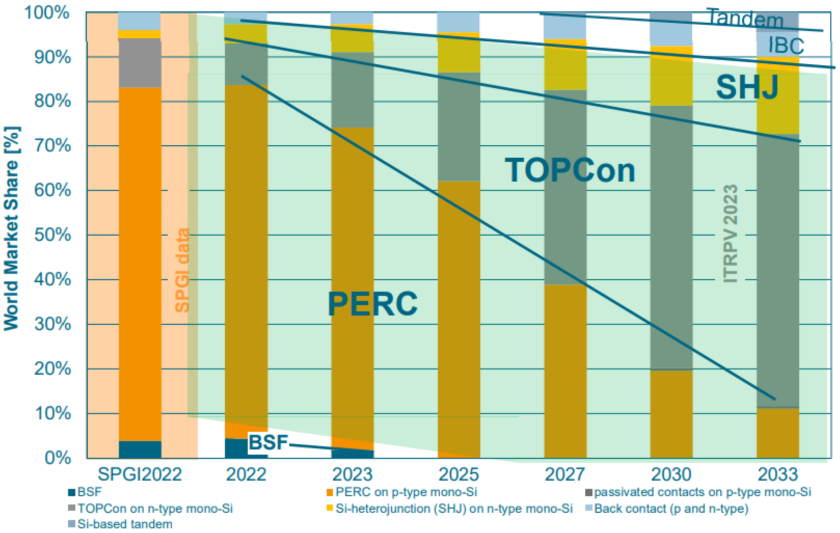

Figure 1.1 - Market shares' trend for various c-Si cell technologies. ITRPV 14th edition, March 2023[5].

From Figure 1.1 we can see that, last year, PERC technology presented itself as the main technology used in industry, boasting a market share of almost 80%. However, current trends show a gradual decline, being predicted that by 2033 its market share will go down to around 10%. In contrast, TOPCon and SHJ technologies are still growing, although at different rates. TOPCon ended 2022 with a market share of around 10%. However, its compatibility with existing solar cell manufacturing processes, coupled with increasing research and development, is making production become more optimized, so the cost of making these cells is becoming competitive. With this, it is expected that by 2033, the market share for this technology will increase to 60%. As for SHJ, its journey holds a slower ascent, since it is still emerging in industry. Still, from a modest 3% of market share last year, SHJ is predicted to increase to roughly 20% in 2033. The Power Conversion Efficiency (PCE) record for SHJ-SC is, at the moment, 26.81%[9]. This technology is primed for substantial growth due to continuous research and development efforts, focused at improving both the technology and manufacturing processes. In this work, the focus will be on the SHJ technology.

1.3 Silicon Heterojunction Solar Cell

Silicon heterojunction solar cells (SHJ-SC) are based on an interface between two distinct semiconductor materials, commonly amorphous and crystalline silicon, leading to the formation of the so-called heterojunction. When sunlight reaches the cell, electron-hole pairs are excited. These carriers are effectively selected by the heterojunction configuration, preventing premature recombination. This means that at each of the two heterojunctions (front and rear) there is an uneven population of electrons or holes that can be available for current generation, contributing to the cell's higher performance. Figure 1.2 represents the full solar cell's schematic of the silicon heterojunction cells that were fabricated during this project.

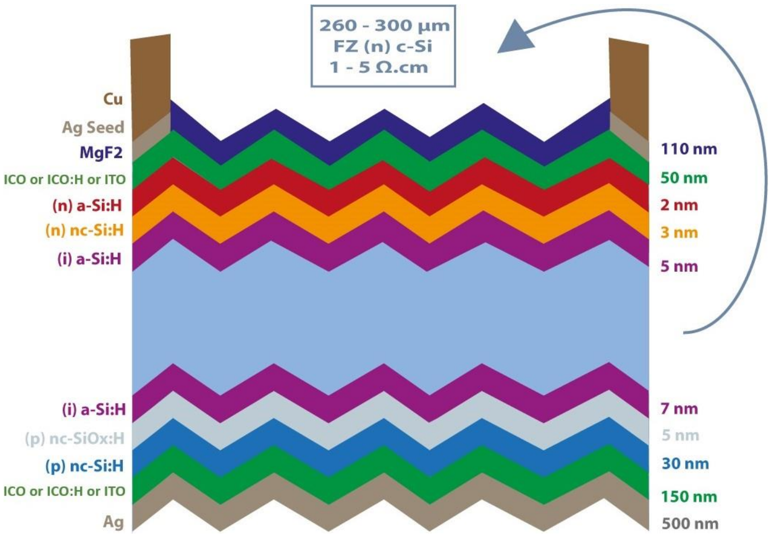

Figure 1.2 - Schematics of the silicon heterojunction solar cells fabricated in this work.

A critical configuration emerges in the context of SHJ contact stack topologies. This configuration includes both intrinsic (i) and doped (n/p-) a-Si:H thin layers. The intrinsic layers are crucial for effective chemical passivation to the c-Si surface[10] but also for constituting the first layer of the selective carrier stack[11,12]. The doped layers must present low activation energy for both contacts to decrease the energy barrier for which electrons or holes can be selectively transported across the heterointerface; and a higher bandgap than that of intrinsic a-Si:H is also recommended for hole collection in the p-contact[13]. This arrangement incorporates a hydrogenated nanocrystalline (nc-Si:H) layer to function as carrier-selective contact (CSCs)[14–16]. Notably, when combined with oxygen (nc-SiOx:H), it facilitates controllable optical and electrical properties[17,18]. As for the transparent conductive oxide (TCO), high conductivity and high transparency is required. It is also important that the TCO presents high mobility and low contact resistance with adjacent layers (minimum carrier concentration of ~10^{20} cm^{-3} [19]). The applied MgF_2 layer forms, together with the front TCO, a double anti-reflection coating. Finally, the metal electrode should present high aspect ratio and low finger resistivity[20,21].

1.4 Transparent Conductive Oxides (TCOs)

One of the most critical layers to optimize is the TCO layer, since it is responsible for more effective charge collecting and light transmission. When applied as front window, it must let incoming sunlight into the absorber and excite electron-hole pairs, guaranteeing that a considerable percentage of sunlight reaches the cell's absorbing layers. But, because it is in close touch with the metal fingers, it must be sufficiently conductive to provide a low-resistance path for the carriers through it. TCOs based on In_2O_3 are go-to materials to obtain high mobilities, and one of the most known and used In_2O_3-based TCOs is Indium Tin Oxide (ITO). In the PVMD group, a 75 nm-thick ITO layer presents a mobility of 28 cm^2/Vs and a resistivity of $4.7\times10^{-4}\ \Omega \cdot cm$ [22]. ITO's performance is, however, diminished due to parasitic free carrier absorption and reflection of light, mainly in the NIR.

To overcome these problems, other doped-indium oxides are investigated. Han, C., et al. assessed and compared the performance of two other indium oxide-based TCOs with ITO: tungsten-doped indium oxide (IWO)[23], and hydrogenated fluorine-doped indium oxide (IFO:H)[22]. Firstly, the performance of IWO for improved current in SHJ-SC was studied. When compared to ITO-based reference cell, IWO-based SHJ cell showed an enhancement in its visible (VIS)-NIR optical response. Moreover, by applying an MgF_2 layer on top, the cell had efficiency of 22.92%. Secondly, the performance of IFO:H for passivating contacts c-Si SC was investigated, and broader optical band gap (3.85 eV) and higher mobility were obtained with the IFO:H film in comparison with the ITO film. The final cell showed an efficiency of 21.1%. Other materials have also been considered to replace tin (Sn) in ITO. An electron mobility of ~110 cm^2/Vs was obtained for a 60-nm-thick Zirconium-doped In_2O_3 layer deposited by RF (Radio Frequency) sputtering[24]. Moreover, a mobility of ~150 cm^2/Vs was obtained by the same sputtering process for a 100-nm-thick hydrogenated In_2O_3 layer[25].

Another material that is now being currently explored is Cerium-doped indium oxide (ICO). In this work, the sputtering of cerium-doped indium oxide will be optimized, and this material will then be applied in SHJ-SC. Extensive study has been devoted to looking into the electronic properties of CeO_2. This focus arises from significant changes in the electronic configuration driven by the existence of oxygen vacancies and the reduction of Ce^{4+} to Ce^{3+} ions. This liberation of oxygen is linked to the Ce sites' ability to undergo reversible conversion between the +4 and +3 oxidation states[26]. Furthermore, the ionic radius of Ce^{4+} roughly approximates that of In^{3+} (both with coordination number of 6), resulting in less microstrain next to dopant sites[27]. Its wide bandgap of >3.6[28,29] allows a broader portion of the solar spectrum to go through the TCO, reaching the underlying silicon absorber layers [30].

ICO recently presented a mobility of 170 cm^2/Vs when deposited by Reactive Plasma Deposition (RPD)[31]. When deposited by ion plating with dc arc-discharge, with substrate temperature of 150 °C, mobilities of 130–145 cm^2V/s have been reported[27,32]. As for RF magnetron sputtering, Dey, K., et al.[28] reported a mobility of 71 cm^2/Vs for ICO when deposited with a substrate temperature of 160 °C. Heating the substrate helps in achieving these mobilities due to improved crystallinity, however, due to equipment restrictions, all the depositions done in this work were performed at room temperature. For a RF magnetron sputtered ICO layer deposited at room temperature, a 51.6 cm^2V/s mobility has been shown by An, S., et al.[29].

Two critical metrics may be used to determine the best properties of a TCO film: electrical sheet resistance (Rs) and optical transmittance (T). Thicker TCO films have lower sheet resistance, however they present lower optical transmittance. As a result, the effectiveness of a TCO is dependent on the careful balance of these properties. To achieve this balance, a Figure of Merit (FOM) can be introduced. The FOM used in this work was proposed by Haacke[33], and is mathematically described as $FOM = \frac{T_{AVG}^{10}}{R_s}$, with T_{AVG} being the average transmittance in the wavelength range of interest, and R_s the sheet resistance of the film. A greater FOM suggests a better compromise between TCO transparency and conductivity, which eventually contributes to better solar cell performance.

1.5 Objectives

In this work, deposition parameters of RF magnetron sputtered ICO were optimized in order to improve the optoelectrical properties of this material to be employed in SHJ-SC. Since one key goal of laboratory research is to be able to upscale the work to be industry compatible, RF magnetron sputtering is employed, since it is an easily scalable deposition technique. Its adaptability to different scales of production is of significant advantage, allowing for seamless transitions from research-focused experiments to commercial application. The optimized parameters in this work were the oxygen flow during deposition, the chamber pressure, the sputtering power, and the water vapor partial pressure. A post deposition annealing was also employed to check for the temperature effect on this material's properties.

2

MATERIALS AND METHODS

2.1 ICO Deposition on 4' Glass

35-nm-thick layers of ICO were deposited onto 10 × 10 cm^2 Corning Eagle 2000 glass by RF magnetron sputtering, with an 81.073 cm^2 target composed of In_2O_3 (97 wt%) and CeO_2 (3 wt%). Before all depositions, the glass substrates underwent a 20-minute ultrasonic cleaning process, with 10 minutes in an acetone bath followed by 10 minutes in an isopropyl alcohol bath. After this, the substrates were dried with nitrogen gas.

Several deposition parameters were varied to obtain the optimum setpoints for the deposition. First, the oxygen partial pressure was varied, followed by pressure, sputtering power and, finally, water vapor partial pressure. The effects of post-deposition annealing at 180 °C in an oven on optical and electrical properties were also investigated. The effects of substrate temperature were not carried out since the heater from the magnetron sputtering equipment was not functional, so all the depositions were performed at room temperature. The total $Ar+O_2$ flow was maintained at 20 sccm.

2.2 Solar Cells' Fabrication

Five silicon heterojunction solar cells were fabricated, varying only the TCO: two with ICO, two with ICO:H, and one with ITO as reference.

First, float zone silicon wafers were dipped in an etching solution containing TMAH, H_2O and AT8 for 15 min at ~82 °C for double-side texturing. The samples were then rinsed in water for 5 min and dried for 9 min. After, they were dipped in acetone for 30 min in order to remove the rest of organic solvents and dried in air. Lastly, the wafers went through wet chemical oxidation process to remove native silicon oxide, where they were dipped in HNO3 99% for 10 min and in HNO3 69% for also 10 min, being water rinsed in between and after for 5 min. Finally, they were dried for 10 min. Right before going to the Plasma-Enhanced Chemical Vapor

Deposition (PECVD) setup, the wafers went through the Marangoni cleaning process, where they were dipped for 5 min in 0.55% HF.

The deposition of ICO or ICO:H or ITO by RF magnetron sputtering and the metallization process by copper plating were performed later by other group members. For TCO, a 50-nm-thick (150-nm-thick) ICO or ICO:H or ITO layer was applied at the front (back) of the solar cell. The rear thickness of ICO or ICO:H was employed according to the deposition rate obtained, but it could be slightly different since it was not tested previously to the deposition. For curing purposes, after the TCO sputtering on the devices, the cells were annealed for 5 min in air at 180 °C. A 110-nm-thick MgF_2 layer was e-beam evaporated on the front side of the final devices for double layer anti-reflecting coating (DLARC) purposes. A full schematic of the fabricated devices with the thickness of each layer is illustrated in Figure 1.2.

2.3 Characterization

The optoelectrical properties of the deposited ICO films were determined after every run of depositions. Spectroscopic Ellipsometry (SE) M-2000DI system (J.A. Woollam Co., Inc.) was used to determine the thickness of the deposited film (fitting the data using the Cody-Lorentz model). Optical properties as transmittance (T) and reflectance spectra were obtained from a spectrophotometric PerkinElmer Lambda 1050 system with total integrating sphere. Finally, to measure sheet resistance, the four-point probe (4PP) method was used, and a Hall measurement setup was used to measure mobility. Carrier concentration and resistivity were first measured by Hall, but later it was noticed that the equipment was not measuring these values correctly, so they were calculated based on theoretical equations. Finally, Haacke's Figure of Merit (FOM) was determined for each deposition run, and the following depositions were adjusted taking this value into consideration. This FOM is mathematically described as:

$$FOM = \frac{T_{AVG}^{10}}{R_s}$$

with T_{AVG} being the average transmittance in the wavelength range of interest, and R_s the sheet resistance of the film. The average transmittance was calculated by integrating the whole spectrum, from 300 nm to 1200 nm, and dividing it for 900 nm (the wavelength range). To check uniformity, thickness and sheet resistance measurements were performed in different parts of the samples, as shown respectively in Figure A.1. In the corresponding plots, the average deviation is represented with an error bar. The solar cells' characterization was also performed later by other group members. Measurements of minority carrier lifetime (τ_{eff}), implied open circuit voltage (i-V_{oc}), and implied fill factor (i-FF) were carried out using the lifetime tester WCT-120 from Sinton Instruments. The current density-voltage (JV) curves were obtained from an AAA class Wacom WXS-90S-L2 solar simulator, and the external quantum efficiency (EQE) measurements were performed using a home-built EQE setup.

3

RESULTS AND DISCUSSION

3.1 RF Magnetron Sputtered ICO

3.1.1 Oxygen Flow

The oxygen partial pressure is expressed as the oxygen gas flux divided by the inert gas flux (argon). The oxygen vacancies present in the films are good scattering sites in the form of ionized impurities that lower the mobility, thereby reducing the conductivity of the material[27,28,34,35]. By using oxygen during sputtering deposition, the transparency of the films increases due to lower optical losses by compensating a significant amount of oxygen vacancies in the thin films. However, due to the lower amount of oxygen vacancies, the carrier concentration will also decrease, which leads to films with higher resistance. Oxygen is quite a significant factor in sputtering and needs to be carefully balanced, so a study of this parameter should be carried out to obtain the best tradeoff between transmittance and conductivity.

A total Ar+O_2 flow of 20 sccm was maintained to ensure low pressures. The oxygen partial pressure effects on ICO films' properties were evaluated by varying the gas mixture composition in the deposition chamber. The oxygen content was varied between 1 sccm and 9 sccm, with an equal step of 2 sccm. Deposition with pure Argon atmosphere was also compared. This deposition series was performed at room temperature, with no intentional heating. Since the equipment's heater could not be fixed by the time this project was over, all the following depositions were also performed at RT. The chamber pressure was kept at 4.0×10^{-3} mbar and the deposition power was 45 W. Finally, the deposition time was 2400 s, except for the processes following the power series. These parameters were based on previous optimization with IWO in the PVMD group.

3.1.1.1 Optical Characterization

For the first deposition series, by using a deposition time of 2400 s for all samples, we obtained thicknesses around 35 nm. Since this represents quite a slow rate of deposition, it was decided to maintain the optimization for a 35-nm-thick film.

From Figure 3.1, we can see that by introducing oxygen in the chamber during deposition, an increase in deposition rate was obtained, from 0.85 to 0.90 nm/min.

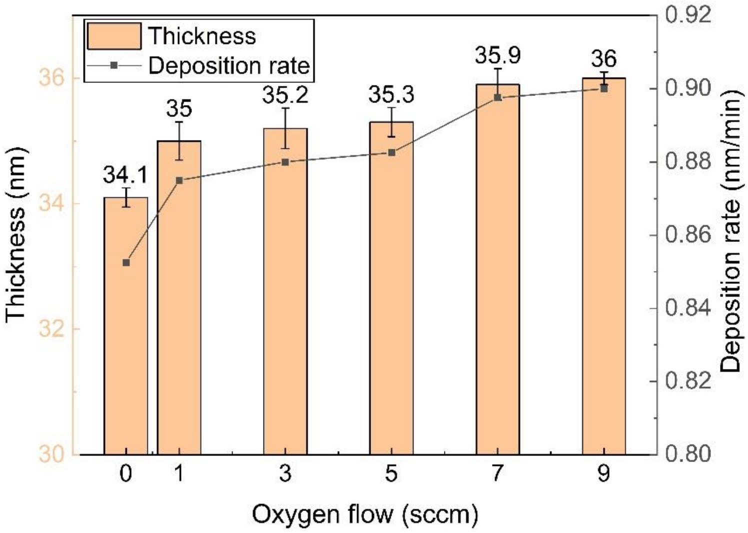

Figure 3.1 - Thickness and deposition rate for the oxygen flow series.

The transmittance spectra are consistent for all the deposited films due to the very small differences in thickness, as we can see in Figure 3.2-a. The disturbance observed in all measurements at 860 nm is a calibration error derived from the equipment.

Figure 3.2 displays the average transmittance of the films with increasing oxygen content, as well as the conductivity, to study the trade-off between this property and transmittance. Conductivity (σ) was deducted from the resistivity (ρ), for $\sigma = 1/\rho$. The average transmittance was calculated by integrating the whole spectrum, from 300 nm to 1200 nm, and dividing it for 900 nm (the wavelength range).

As mentioned above, the introduction of oxygen reduces the amount of oxygen vacancies, reducing parasitic optical losses and increasing transparency. However, these results indicate that the transparency of the films was not very sensitive to the oxygen content, having a slight decrease in the visible range. Changes in oxygen content could have led to new absorption features in the visible range. Further analysis is needed to have a better understanding of the relationship between oxygen content, film properties, and optical behavior, such as X-ray photoelectron spectroscopy (XPS) in order to assess film composition and impurity levels, and UV-VIS spectrophotometry to check for the absorption spectra.

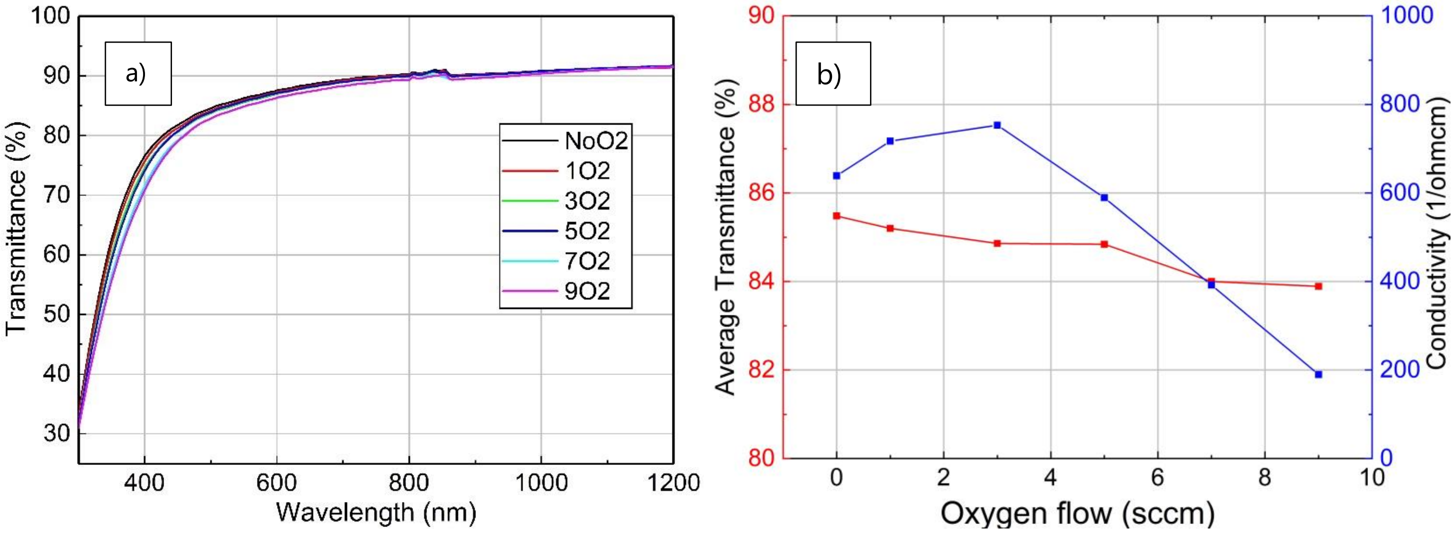

Figure 3.2 - a) Transmittance and b) average transmittance and conductivity for the oxygen flow series.

As for conductivity, the maximum value is obtained with an oxygen flow of 3 sccm. As expected, higher oxygen content led to lower conductivities. These low conductivities result from an increase in resistance caused by a decrease in carrier concentration as oxygen vacancies are filled, as we can observe in Figure 3.3.

The best average transmittance obtained was 85.48 % for the sample with no oxygen content. However, conductivity reaches its best value of 753.10 1/Ω·cm for the sample deposited with 3 sccm of O_2. Taking this into account, and the average values for transmittance, we note that the best trade-off between these two properties is obtained for the sample deposited with 3 sccm of oxygen, with an average transmittance of 84.86 %.

3.1.1.2 Electrical Characterization

Figure 3.3 shows electrical properties (mobility, carrier concentration and resistivity) obtained with increasing oxygen flow during deposition. To calculate the resistivity, sheet resistance measurements (R_{SH}) were used in combination with the thickness (t) measurements, using $\rho = R_{SH} \times \mathrm{t}$. The sheet resistance plot for this series, as well as its error bars, can be seen in Figure A.2. Carrier concentration (N) was calculated with the equation $\mathrm{N} = \sigma/(q \cdot \mu)$, where q is the elementary charge (1.6×10^{-19} C) and μ the mobility.

In low-oxygen conditions, the carrier concentration is higher due to the oxygen vacancies. As oxygen content in the chamber increases, these vacancies are reduced, so the carrier concentration ends up decreasing as well. This explains the higher resistivities obtained for higher values of oxygen flow, since the number of oxygen vacancies is lower, lowering the carrier concentration, and resulting in films with higher resistivity. The resistivity of the films reached its lowest value of $1.33 \times 10^{-3}\ \Omega \cdot cm$ when deposited with an oxygen flow of 3 sccm.

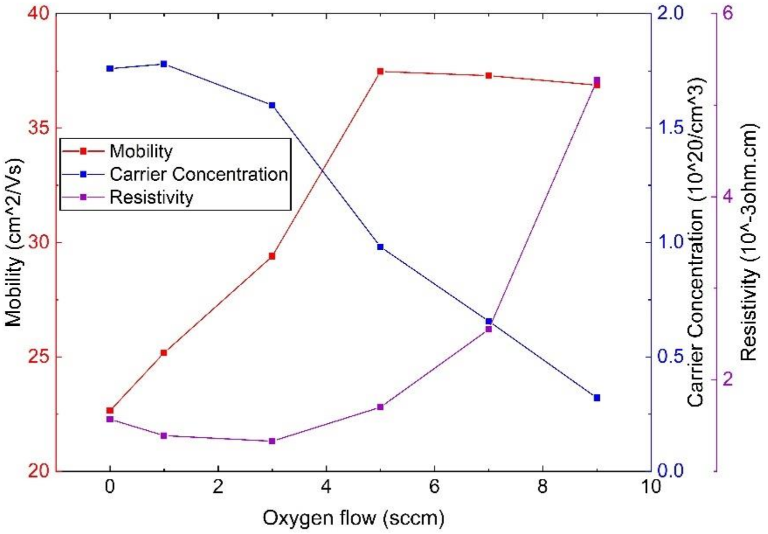

Figure 3.3 - Mobility, carrier concentration and resistivity values for the oxygen flow series.

As for mobility, as reported by others[28,34], it initially increases, but, when we start to have higher oxygen contents, mobility values start to decrease. This decrease could be due to collisions between particles with oxygen as they approach the substrate surface, which can lead to films with poor crystallinity, thus lower mobility. XRD measurements could be performed in order to assess this behavior.

The highest mobility obtained was 37.47 cm^2/Vs for an oxygen flow of 5 sccm. However, using an oxygen flow of 3 sccm gives the best tradeoff between transmittance and conductivity, also ensuring a higher carrier concentration. With this, we continue with a mobility of 29.4 cm^2/Vs, and a carrier concentration of $1.60 x 10^{20}/cm^3$.

3.1.1.3 Figure of Merit

Table 3.1 shows the values for average transmittance and sheet resistance of each sample in order to compare its Figure of Merit (FOM).

Table 3.1 - Figure of Merit for the oxygen flow series.

Oxygen Flow (sccm)	Average Transmittance (%)	Sheet Resistance (Ω/sq)	Fom ($x10^{-4}$)
0	85.48	458.98	4.54
1	85.20	398.55	5.06
3	84.86	377.23	5.13
5	84.84	483.53	4.00
7	84.00	708.49	2.47
9	83.89	1463.76	1.18

As predicted before, the highest FOM for this deposition series is achieved with an oxygen flow of 3 sccm, so the following optimizations were performed using this value of oxygen flow. This film presented a thickness of 35.2 nm, and its deposition rate was 0.88 nm/min.

3.1.2 Chamber Pressure

From this point on, the carrier concentration decreased, and this was most likely due to contamination of the chamber with oxygen. This contamination could have come from the constant changing of the equipment's target, since there were other materials being deposited. Nevertheless, it is important to assure $N > 10^{20}$ cm^{-3} for device integration to achieve low contact resistance with adjacent layers[19].

The chamber pressure in magnetron sputtering has a direct influence on the ultimate performance and attributes of the deposited thin film. If the pressure used during deposition is too low, there is a decrease in ion flux at the target, and so the plasma needed for the procedure may not be sustained in this condition. If the pressure is too high, for example, a decrease in the deposition rate can occur, since there is an increase in the amount of collisions experienced by sputtered particles directing to the substrate.

Within the pressure series, the chamber pressure range used was from $2.6 x 10^{-3}$ mbar (lowest value that the equipment achieved) to $6 x 10^{-3}$ mbar. A larger range was previously tested but higher pressures led to a far greater degradation.

3.1.2.1 Optical Characterization

First of all, from Figure 3.4, we can see that, for the same pressure used in the previous optimization, and using the same deposition time, the deposition rate decreased. There could be two reasons for this: one, since the chamber could be contaminated with oxygen, higher contents of oxygen during deposition has been reported[36] to decrease the deposition rate due to the existing oxidation-rich environment, which can result in the development of oxides on the target surface, that can then be sputtered onto the substrate. As a result, the deposition rate may drop due to the increased possibility of sputtering oxides rather than the desired material; two, the spectroscopic ellipsometry setup was later reported to not have been measuring the thickness with much precision, especially such thinner films.

Higher pressures can decrease the deposition rate due to sputtered particles undergoing more collisions on their path to the substrate, but from ITO literature[36] and from Figure 3.4, we can see that increasing the pressure increased the deposition rate, in this case from 0.82 to 0.86 nm/min.

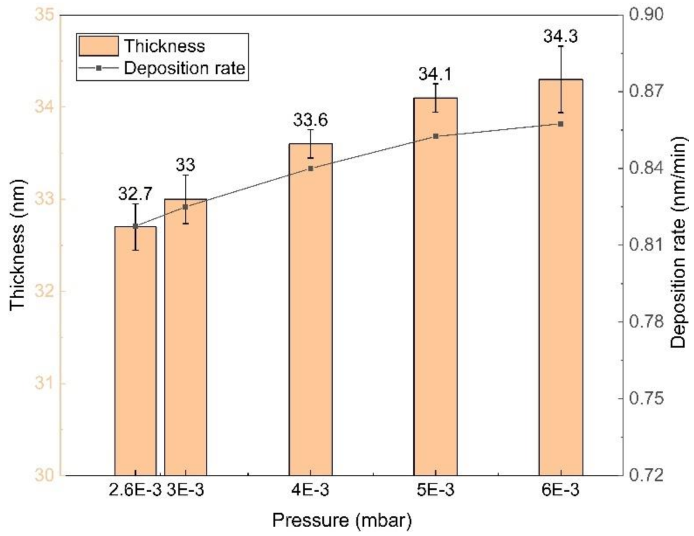

Figure 3.4 - Thickness and deposition rate for the chamber pressure series.

The transmittance spectra with increasing background pressure, as well as conductivity and the average transmittance of the films, are displayed in Figure 3.5.

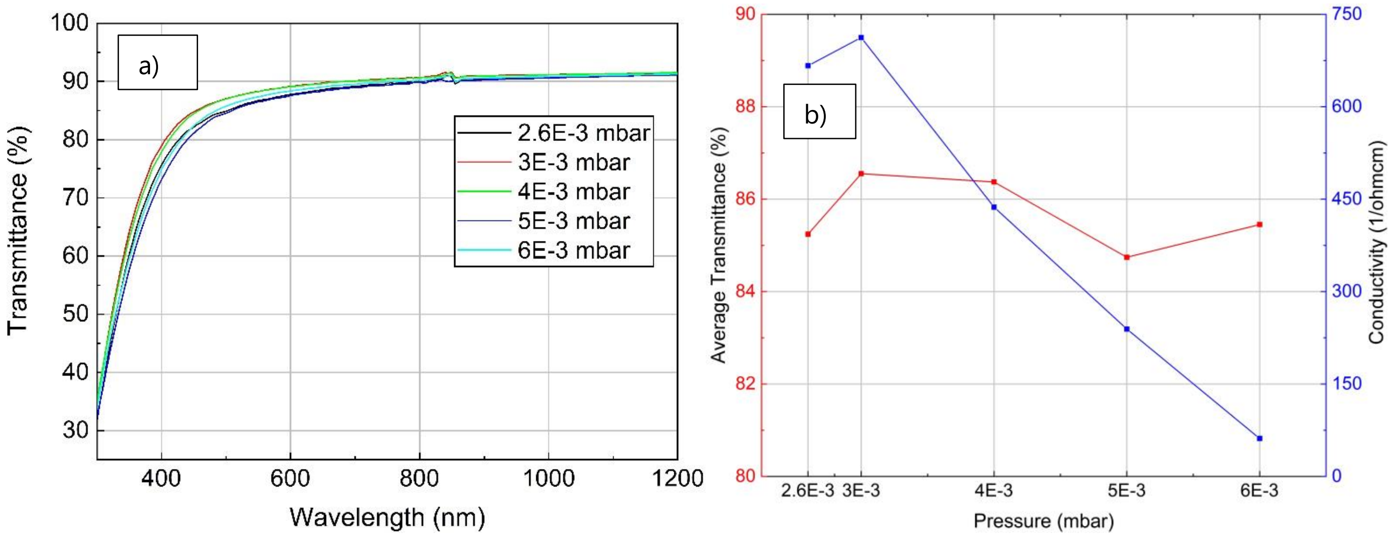

Figure 3.5 - Transmittance and b) average transmittance and conductivity for the chamber pressure series

Transmittance was not very sensitive to the chamber pressure, having only slight random variations in the average transmittance. A pressure of $3 \times 10^{-3}\ mbar$ presented the best average transmittance, and higher pressures increase the probability of collisions experienced by sputtered particles, so there could have been integration of additional defects (such as voids or impurities). If this is what is happening, then these defects could be scattering/absorbing light, lowering the film's total transmittance.

As for conductivity, we can see that it also initially improved and then decreased sharply for pressures higher than $3 \times 10^{-3}\ mbar$. This decreased can be attributed to the low carrier concentration due to low sputtering yield (number of atoms ejected from the target for each incident ion) at higher pressures.

The best average transmittance obtained was 86.55 % for the sample deposited with a chamber pressure of $3 \times 10^{-3}\ mbar$. Moreover, conductivity reaches its best value of 712.12 1/Ω·cm for the same sample. This conductivity value is lower than the previous one obtained for the oxygen series, but again we had a change in the bulk concentration.

3.1.2.2 Electrical Characterization

Figure 3.6 shows the mobility, carrier concentration and resistivity values obtained with increasing chamber pressure. For pressures higher than $3 \times 10^{-3}\ mbar$, the resistivity starts to increase due to the low sputtering yield at higher pressures. This low sputtering yield lowers the amount of sputtered atoms that reach the substrate, reducing the carrier concentration. Also, with this lower energy of the gas molecules, the crystallinity of the film can be degraded, since crystallinity often requires a certain level of energy for atoms to rearrange themselves into a well-defined crystal lattice, so this lower energy may not be sufficient to achieve this structure. Less crystallinity in a material introduces disorder, disrupting ordered pathways for charge carriers, and increasing scattering. These factors collectively reduce carrier mobility and increase resistivity. This can also explain the increase in the error bars for sheet resistance with increasing pressures (Figure A.3) as the films may exhibit non-uniformity.

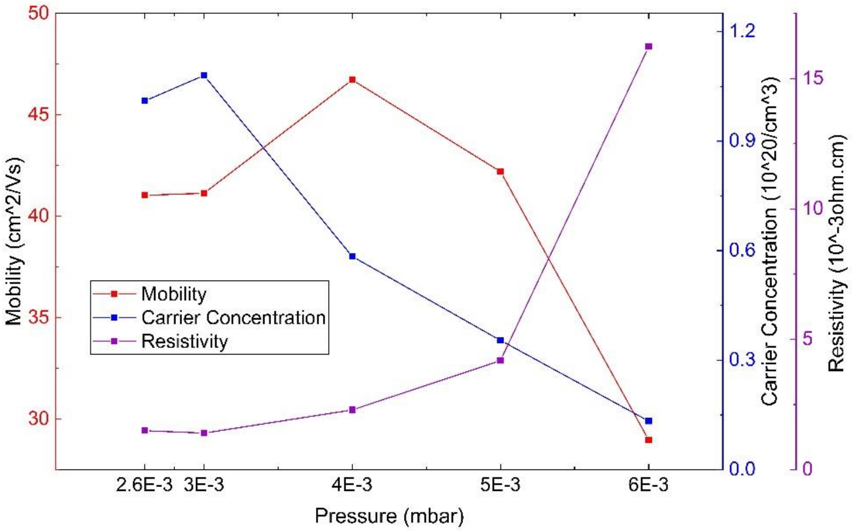

Figure 3.6 - Mobility, carrier concentration and resistivity values for the chamber pressure series.

Even though the highest mobility obtained was 46.72 cm^2/Vs for the sample deposited at a pressure of $4 \times 10^{-3}\ mbar$, the best tradeoff between transmittance and conductivity was for the sample deposited at $3 \times 10^{-3}\ mbar$. Also, resistivity presented its lowest value of $1.4 \times 10^{-3}\ \Omega \cdot cm$ with this pressure. With this, we continue with a mobility of 41.13 cm^2/Vs, and a carrier concentration of 1.08x10^{20}/cm^3.

3.1.2.3 Figure of Merit

Table 3.2 shows the values for average transmittance and sheet resistance for the different samples deposited with increasing chamber pressure to compare its figure of merit.

Table 3.2 - Figure of Merit for the chamber pressure series.

Chamber Pressure (mbar)	Average Transmittance (%)	Sheet Resistance (ohm/sq)	FOM ($x10^{-4}$)
2.6E-3	85.24	458.83	4.41
3E-3	86.55	425.53	5.54
4E-3	86.37	681.12	3.39
5E-3	84.74	1226.74	1.56
6E-3	85.45	4727.43	0.44

The highest FOM for this deposition series is achieved with a chamber pressure of $3 \times 10^{-3}\ mbar$. This film presented a thickness of 33 nm and a deposition rate of ~ 0.83 nm/min.

3.1.3 Sputtering Power

The energy of the ions bombarding the target material is affected by sputtering power, resulting in more energetic collisions, so the particles expelled from the target have higher velocities. Higher velocities translate to more momentum and faster transit to the substrate, resulting in a faster deposition rate. The increased frequency of collisions with increased sputtering powers enhances the sputtering yield, leading to higher film density[37,38], which can result in enhanced mobility and atom rearrangement during deposition. However, higher film density might compromise the optical transparency of the film, due to increased light scattering at interfaces and grain boundaries.

With the pressure outcome, we followed using $3 \times 10^{-3}\ mbar$ in this series. Five depositions with sputtering power varying from 30 to 90 Watt with a step of 15 Watt were done to verify the effects of increasing sputtering power in the film's electrical and optical properties. First, a batch was done to check the deposition rate with different sputtering powers. Later, another batch was made so all the thicknesses of the films could be similar in order to compare the effects of the sputtering power.

3.1.3.1 Optical Characterization

Figure 3.7 displays the thickness and deposition rate variation for increasing sputtering power. The correlation between deposition rate and sputtering power appears to be approximately linear, increasing from 0.62 nm/min at 30 W to 1.86 nm/min at 90 W. The error bars for thickness appear to be relatively consistent for the various powers, implying that increasing power is not affecting uniformity.

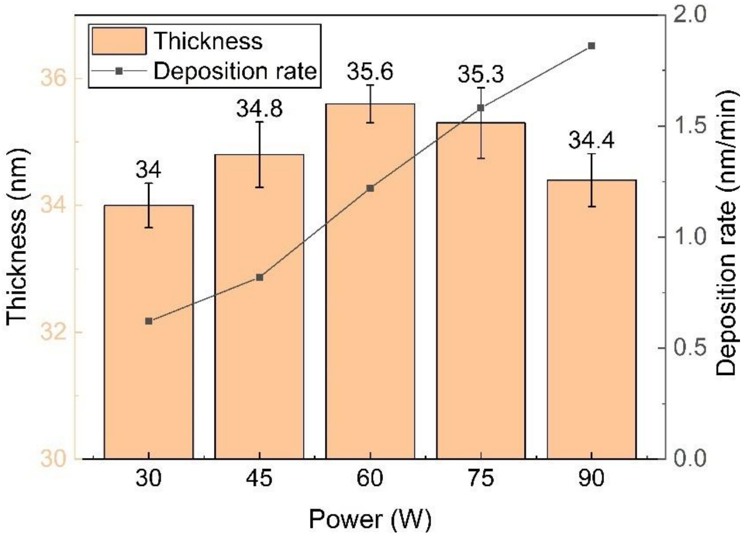

Figure 3.7 - Thickness and deposition rate for the sputtering power series.

Figure 3.8 displays the transmittance spectra and the average transmittance and conductivity of the films with increasing sputtering power.

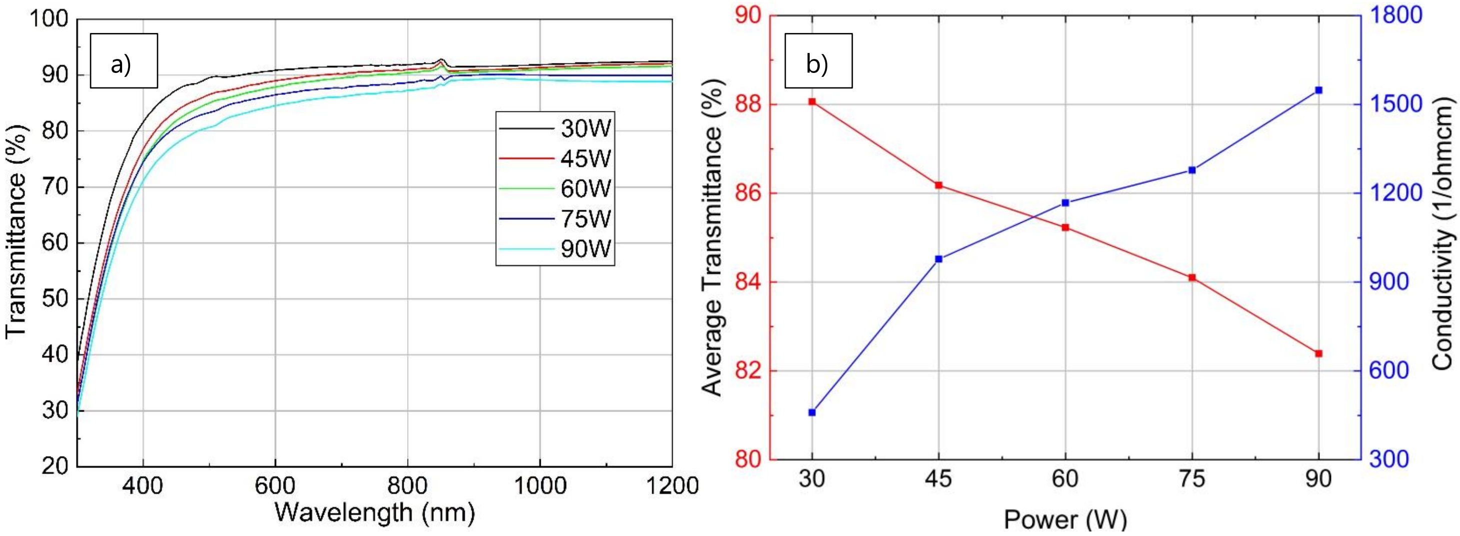

Figure 3.8 - a) Transmittance and b) average transmittance and conductivity for the sputtering power series.

As expected, increasing the power led to a decrease in transmittance in all the wavelength range. From Figure 3.9 we can see that the carrier concentration increased with higher sputtering power values, and this affects the transmittance of the films. As mentioned above, the possible higher film density with increasing power might compromise the optical transparency of the film due to increased light scattering at interfaces and grain boundaries, but can increase the conductivity by lowering the resistivity, which is corroborated in Figure 3.9 where we see a decrease in resistivity.

The best average transmittance obtained was 88.06 % for the sample deposited with the lowest sputtering power, and conductivity reached its best value of 1547.89 1/Ω·cm for the sample deposited with the highest sputtering power. The best trade-off between these two properties was obtained for the intermediate power of 60 W, which presented an average transmittance of 85.23 % and a conductivity of 1167.57 1/Ω·cm.

3.1.3.2 Electrical Characterization

Figure 3.9 shows the electrical properties obtained with increasing sputtering power. The resistivity of the films decreased as the sputtering power increased, reaching its lowest value of $6.46 \times 10^{-4}\ \Omega \cdot cm$ for the film deposited with the maximum sputtering power tested (90 W).

From the error bars for sheet resistance (Figure A.4) we can see that increasing power led to more uniform films. Higher power increases the sputtering rate, facilitating consistent target material removal and improving film uniformity. However, we previously saw in Figure 3.7 that the error bars obtained for the thickness measurements were consistent for the various powers, so again the spectroscopic ellipsometry setup was most likely performing exact but not precise measurements.

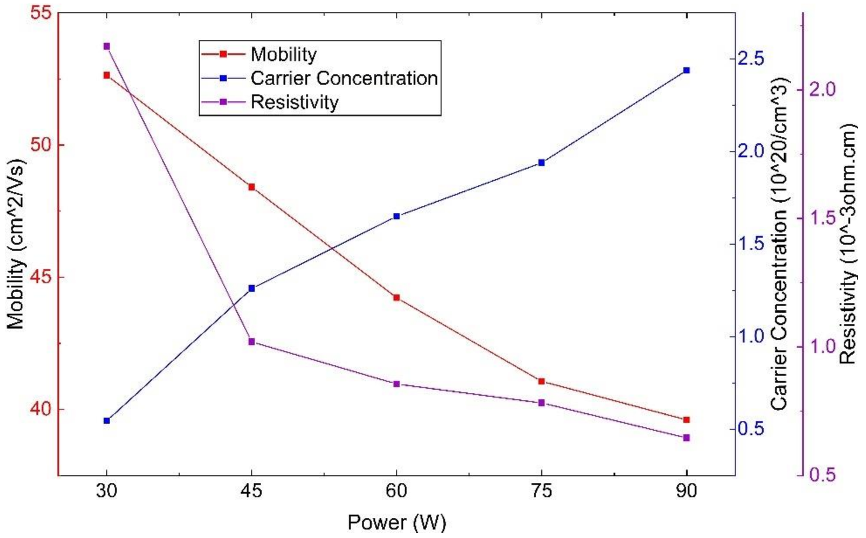

Figure 3.9 - Mobility, carrier concentration and resistivity values for the sputtering power series.

The increased energy of the sputtered particles with increasing power can allow these particles to knock away oxygen atoms from the deposition, lowering the oxygen content and raising the carrier concentration. The formation of a denser film at higher powers leads to smaller crystal structures in the bulk[39], leading to higher conductivity and carrier concentration but lower mobility.

The highest mobility obtained was for the deposition made with the lowest power. However, the carrier concentration is much lower. Considering the results for conductivity and optical transmittance, the best option seems to be to use a power of 60 W for deposition, having a mobility of 44.22 cm^2/Vs, a carrier concentration of 1.65x10^{20}/cm^3, and a resistivity of $8.56 \times 10^{-4}\ \Omega \cdot cm$.

3.1.3.3 Figure of Merit

For the power series, the FOM values are displayed in Table 3.3, presenting its best value for the deposition made with a power of 60 W.

Table 3.3 - Figure of Merit for the sputtering power series.

Power (W)	Average Transmittance (%)	Sheet Resistance (ohm/sq)	FOM ($x10^{-4}$)
30	88.06	639.49	4.38
45	86.18	293.90	7.69
60	85.23	240.58	8.41
75	84.10	221.65	7.99
90	82.39	187.80	7.67

This film presented a thickness of 35.6 nm, and a deposition rate of ~1.22 nm/min.

3.1.4 Hydrogenation

Water vapor during deposition can have a significant effect on numerous properties of the TCO layer. Effectively controlling the water vapor partial pressure is crucial for achieving suitable doping levels[34]. However, using water vapor during deposition can lead to a reaction between this gas and the sputtered material, which can cause the formation of other species that can affect film smoothness and uniformity, lowering the conductivity. When using low water vapor pressures, the likelihood of interactions between this gas and the sputtered material or other chamber is decreased, resulting in a purer, defect-free film with improved electrical properties.

With the power outcome, we followed using a sputtering power of 60 W. For the hydrogenation series, the goal was to test the effects of water vapor partial pressures on the film in the range from $10^{-7}\,mbar$ to $10^{-5}\,mbar$, but the equipment did not go lower than $3 \times 10^{-6}\,mbar$. So three depositions with water vapor partial pressure varying from $3 \times 10^{-6}\,mbar$ to $9 \times 10^{-6}\,mbar$ with a step of $3 \times 10^{-6}\,mbar$ were performed. However, it was also difficult to control the water vapor partial pressure in the chamber, so the values were not steady throughout the entire deposition.

3.1.4.1 Optical Characterization

Figure 3.10 displays the thickness and deposition rate variation for increasing water vapor partial pressure. Within this range, we had a steady deposition rate around 1.20 nm/min.

We can see from the power series that the deposition rate decreased from 1.22 nm/min to 1.20 nm/min when water vapor was introduced during deposition. The presence of water vapor can introduce numerous elements that affect the deposition process, resulting in a slower rate of film development. One of the reasons might be that water vapor can participate in chemical interactions with sputtered species or other species in the deposition environment. These reactions may result in the creation of compounds that are less favorable to film growth which can reduce the deposition rate.

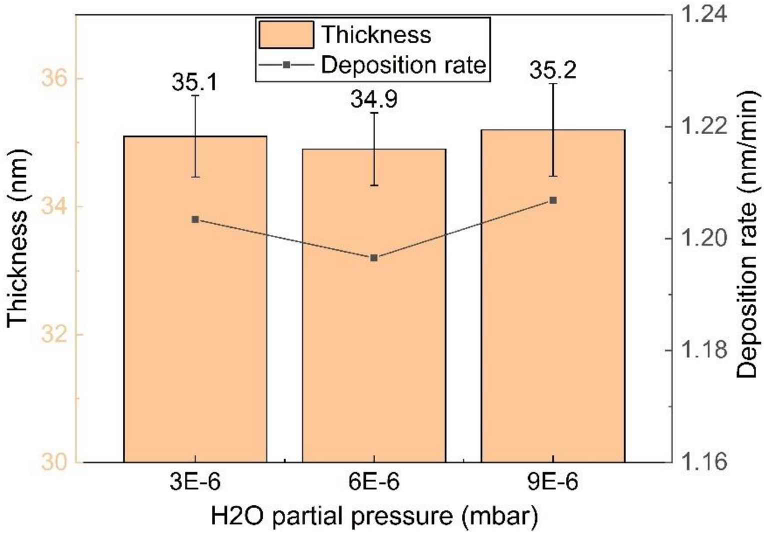

Figure 3.10 - Thickness and deposition rate for the hydrogenation series.

Figure 3.11-a displays the transmittance and reflectance spectra, and Figure 3.11-b the average transmittance and conductivity of the films with increasing water vapor partial pressure. The results for transmittance/reflectance showed that water vapor partial pressure had minimal impact in these properties. When water vapor was introduced, the average transmittance had a minimal decrease of less than 1 %. With increasing water vapor pressure, it seems that the transparency of the films was not much affected, and that perhaps the sample deposited with $6 \times 10^{-6}\ mbar$ was not perfectly clean.

The conductivity decreased with increasing water pressure, so there could have been reactions in the chamber that led to the introduction of flaws or contaminants into the layer, lowering the conductivity. However, the conductivity has increased in respect to the sample deposited with no water vapor in the chamber, and this could be due to higher carrier concentration, as corroborated in Figure 3.12.

The best average transmittance and conductivity obtained was 84.73 % and 1373.781/Ω·cm, respectively, for the sample deposited with the lowest water vapor pressure.

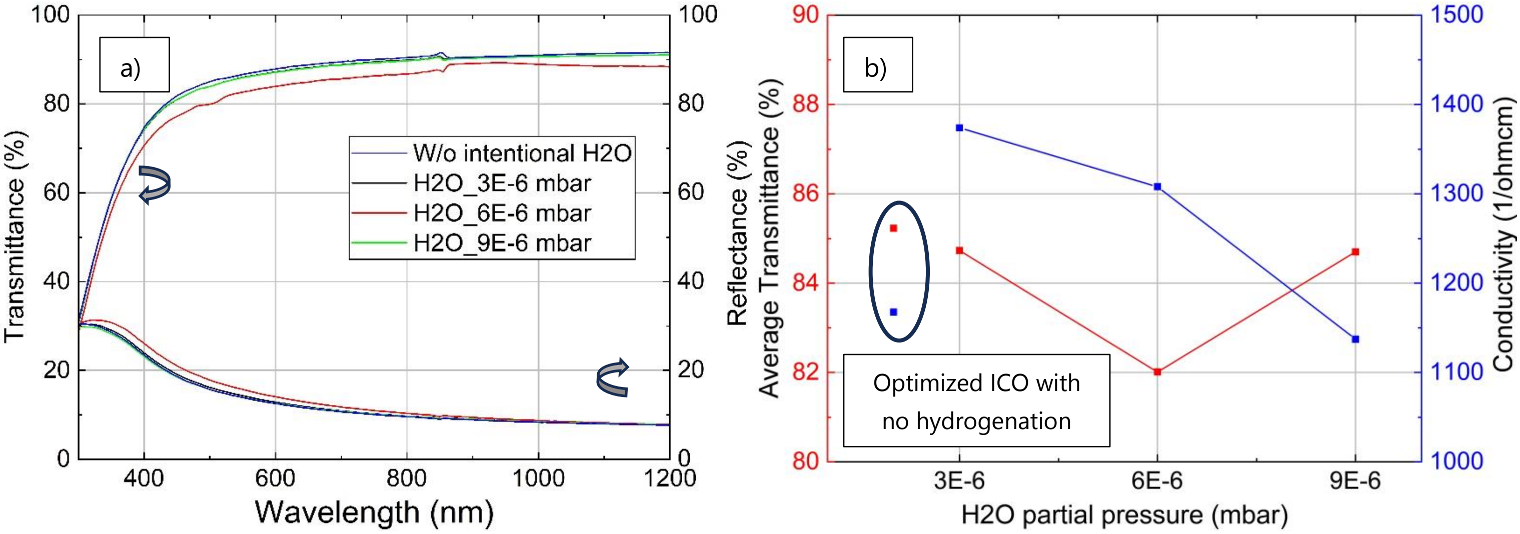

Figure 3.11 - a) Transmittance and b) average transmittance and conductivity for the hydrogenation series.

3.1.4.2 Electrical Characterization

Figure 3.12 displays the values of mobility, carrier concentration and resistivity obtained with increasing water vapor partial pressure. The resistivity decreased when water vapor was introduced in the deposition, and increased with increasing water partial pressure, as explained above. As for the error bars for sheet resistance measurements (Figure A.5), we can see that these measurements were not uniform, and this could be due to the fact that water vapor can change surface morphology, affecting uniformity.

The addition of water vapor to the deposition had minimal impact in the mobility. The increase in carrier concentration in respect to the ICO film deposited with no water vapor was also reported by Tutsch, et al., (2021)[34]. Introducing water vapor in the deposition can lead to the formation of semiconductor-oxygen bonds that passivate the surface, and this may inhibit nucleation of crystalline phases. The formation of an amorphous arrangement results in less lattice defects, which increases the carrier concentration[34]. The further decrease in this property could be due to a high amount of weakly bonded acceptor-type oxygen, and/or to the effective incorporation of oxygen vacancy-type defects due to a more porous structure[34].

The best transmittance and conductivity was for the sample deposited at $3 \times 10^{-6}\ mbar$. Also for this sample, resistivity reached its lowest value of $7.28 \times 10^{-4}\ \Omega \cdot cm$. This sample presented a mobility of 44.56 cm^2/Vs, and a carrier concentration of 1.92x10^{20}/cm^3.

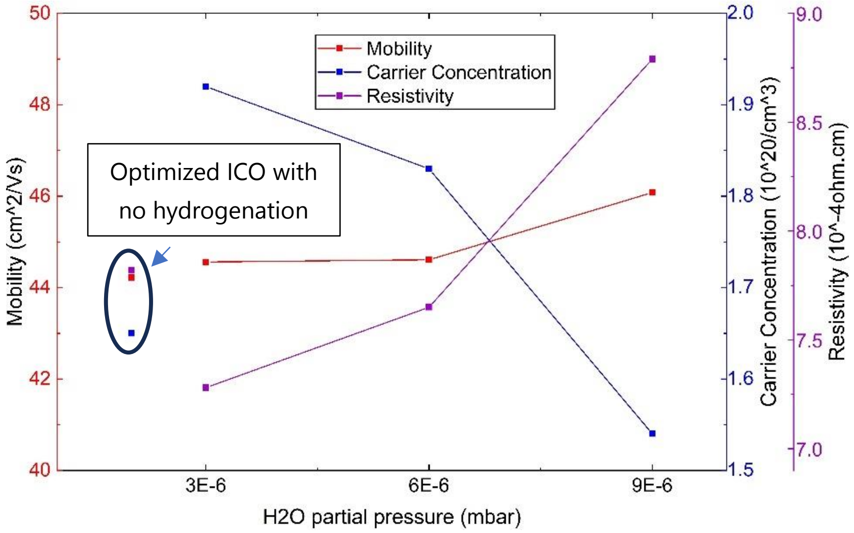

Figure 3.12 - Mobility, carrier concentration and resistivity values for the hydrogenation series.

3.1.4.3 Figure of Merit

Table 3.4 shows the values for average transmittance and sheet resistance for the different samples deposited with increasing water vapor partial pressure to compare its figure of merit.

Table 3.4 - Figure of Merit for the hydrogenation series.

Pressure (mbar)	Average Transmittance (%)	Sheet Resistance (ohm/sq)	FOM ($x10^{-4}$)
3E-6	84.73	207.38	9.20
6E-6	82.01	219.07	6.28
9E-6	84.70	249.83	7.61

The highest FOM for this deposition series is achieved with a water vapor partial pressure of $3 \times 10^{-6}\ mbar$. This film presented a thickness of 35.1 nm and a deposition rate of 1.20 nm/min.

3.1.5 Annealing at 180 °C

Post-deposition annealing in thin films can have a variety of impacts in its characteristics. This process, when performed in the proper conditions, can enhance the crystallinity of the film, leading to bigger and well-defined crystalline grains, lower the amount of defects, improve optical transparency, etc.[34,40,41] The results, however, are affected by annealing conditions, film composition, and intended applications. To obtain the desired outcome while avoiding potential undesirable consequences such as increased defects or phase changes, annealing settings must be carefully controlled. Characterization is critical to ensuring that the produced films fit the standards of their purpose.

Annealing was performed on the best ICO and ICO:H films in an oven at 180 °C for varied time periods. Although a higher temperature generally results in an increased annealing effect[28,40,42], temperatures around 200 °C correspond to the maximal threshold for thermal stability of interface passivation and contact resistivity concerning a-Si:H-based contacts[43,44] in SHJ-SC. Furthermore, it is noteworthy that these time periods were divided into phases rather than being continuous. For instance, the 5-minute annealing consisted of the previous 2 min followed by 3 min more. Similarly, the 10-minute annealing included the preceding 2 min plus 3 min, followed by an additional 5 minutes, and so on. Both electro and optical measurements were performed 30 min after annealing.

3.1.5.1 Optical Characterization

Figure 3.13 shows the transmittance and reflectance spectra for ICO and for ICO:H films with various annealing times. We can see that annealing generally degraded the transmittance for both ICO and ICO:H. Liu, et al. (2023)[40] studied how annealing temperature and annealing time can impact the optoelectrical properties of ICO films produced via RPD at room temperature. They found that the transmittance only improved after an annealing treatment with temperatures above 190 °C, and considered 210 °C as the optimal annealing temperature. Increasing the annealing temperature led to a higher intensity of the diffraction peak associated with the (222) plane, suggesting an enhancement in the crystalline structure of the film. Also, the diffraction peak of the (222) crystal plane shifts to a bigger angle, reflecting a decrease of internal stress in the film.

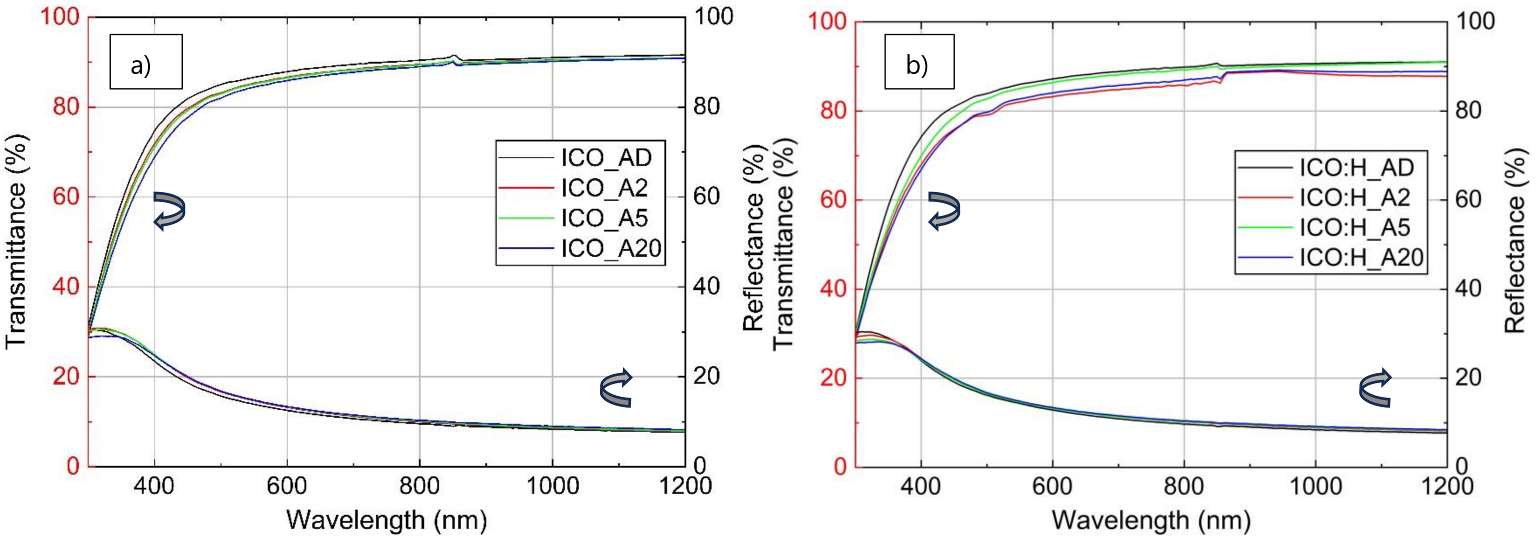

Figure 3.13 - Transmittance and reflectance spectra for a) ICO and b) ICO:H films with increasing annealing time.

As for the annealing time, since our films are only 35 nm, a short period of annealing should be employed to not degrade the film. From Figure 3.13 we can see that for the ICO film, all the annealing periods degraded the transmittance, but annealing for 2 or 5 min did not change this property much. The fact that the film was not continuously annealed for the entire period could be an important factor to be considered, since the cooling step in between the two annealing steps might make changes to the film's properties. Also, from Figure 3.14, we can see that the carrier concentration had minimal changes for these two annealing periods. As for the ICO:H film, with a 2 min annealing the transmittance decreased, then for 5 min it increased, and then decreased again for 20 min, so the most suited annealing time could be in this range. Nevertheless, for the studied annealing periods an increase in transmittance was not observed, most likely due to suboptimal annealing temperature.

Lastly, the results for reflectance in both films show that this property was not affected much by the annealing time, so the decrease in transmittance seems to be due to an increase in absorption. Since no further characterization was performed, we can only speculate that perhaps, since the annealing was performed in air, the specimens present inherently in this environment could have been incorporated into the film during annealing, acting as impurities that contribute to increased absorption. XPS measurements could help to assess this, providing information about the chemical composition of the film's surface.

3.1.5.2 Electrical Characterization

Since sheet resistance was not measured for this optimization, only the mobility values on Figure 3.14 are reliable to check the effect of annealing on the electrical properties, because the carrier concentration values are not correct (due to the aforementioned problem with the Hall equipment). Nevertheless, these values are still shown in Figure 3.14 for the trend could be the same as with the correct values.

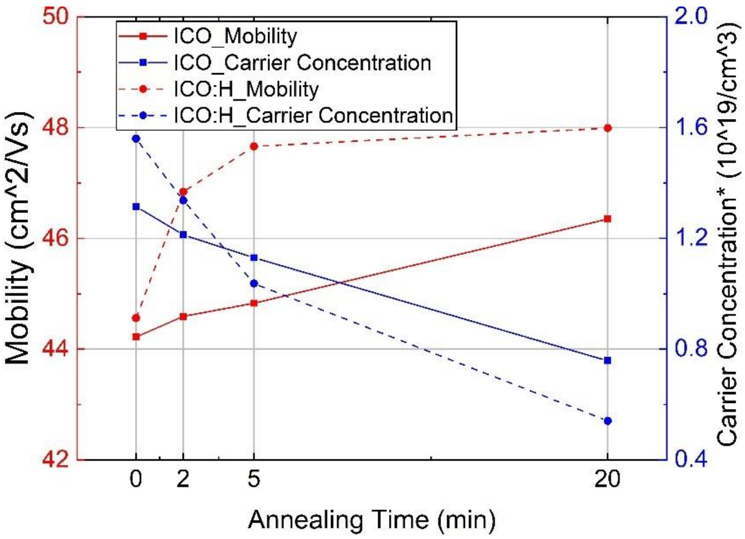

Figure 3.14 - Mobility values and carrier concentration trend for different annealing time periods, both for the ICO and ICO:H film. (*Carrier concentration values are not correct).

From the optical results, we saw that specimens could have been incorporated into the film during annealing due to the air environment. If this is true, these specimens can create charge traps or cause defects, resulting in the decrease of the carrier concentration that is seen in

Figure 3.14 Liu, et al. (2023)[40] also showed that annealing reduced the carrier concentration and increased the conductivity[40], so conductivity measurements could serve as an indicator to assess if this is what is happening, since this property would likely have decreased due to such incorporation of air specimens. This decrease in carrier concentration might be offset by the increase in mobility.

The annealing of this layer during the fabrication of the SHJ devices is nevertheless important for curing purposes, so a 5 min annealing was later employed when making the solar cells. With this annealing time, the ICO film presented an average transmittance of 83.86 % and a mobility of 44.83 cm^2/Vs, and the ICO:H an average transmittance of 83.63 % and a mobility of 47.66 cm^2/Vs.

3.2 SHJ Solar Cell Application

From the TCO optimization, the 35-nm-thick ICO layer presented a mobility of 44.22 cm^2/Vs, a carrier concentration of $1.65x10^{20}/cm^3$, a resistivity of $8.56 \times 10^{-4}\ \Omega \cdot cm$, and an average transmittance of 85.23%. As for the ICO:H with the same thickness, it presented a mobility of 44.56 cm^2/Vs, a carrier concentration of $1.92x10^{20}/cm^3$, a resistivity of $7.28 \times 10^{-4}\ \Omega \cdot cm$, and an average transmittance of 84.73%. When annealed for 5 min, the ICO film presented an average transmittance of 83.86 % and a mobility of 44.83 cm^2/Vs, and the ICO:H an average transmittance of 83.63 % and a mobility of 47.66 cm^2/Vs.

To check the impact of the optoelectrical properties of the optimized TCOs on full solar cells, five SHJ-SC were fabricated, with the only variable being the TCO: two of them were fabricated with ICO, two employing ICO:H, and one featuring ITO as a benchmark. The front TCO is composed of a 50-nm-thick ICO or ICO:H or ITO layer, and the rear TCO is composed of a 150-nm-thick ICO or ICO:H or ITO layer. Copper plating was employed as the metallization process due to its reduced shading losses and finger resistance[45], and a 110-nm-thick MgF_2 layer was e-beam evaporated in the front side as Double Layer Anti Reflecting Coating (DLARC).

3.2.1 Minority Carrier Lifetime, I-FF, and I-V_{OC}

The minority carrier lifetime (τ_{eff}) represents the average time before the minority carriers recombine after photo-induced excitation; so a longer lifetime is desirable for allowing more time for these carriers to travel through the semiconductor, thus enhancing the overall performance of the solar cell. The FF measures how effectively the solar cell converts light into electrical power, being the ratio of the maximum power to the product of the V_{oc} and the short-circuit current (I_{sc}). I-FF represents what the FF would be if the solar cell were to operate at its i-V_{oc} under the given conditions, so it basically represents the theoretical maximum FF achievable by the solar cell. Similarly, the i-V_{oc} is the theoretical maximum V_{oc} that the solar cell can achieve under certain conditions, typically for an injection level of charge carriers close to the injection level observed under one-sun condition.

The measurements of τ_{eff}, i-FF, and i-V_{OC} are displayed in Figure 3.15. These properties were measured before and after TCO sputtering, and as well after the annealing process applied to repair passivation quality. The τ_{eff} was measured at a specific minority carrier density of 1×10^{15} cm^{-3} because at this specific density level, the influence of Auger and radiative recombination on recombination velocity becomes less pronounced, providing insights into the nature of defects[46]. Moreover, this density value closely approximates the injection level observed under one-sun condition[46].

The ICO_#1 cell's minority carrier lifetime is much higher when compared to the other cells. The i-V_{oc} also presents a too high value that should be a measurement error. When measuring the i-V_{oc} and i-FF after annealing, the results for this cell seemed too random, so it was chosen not to present them in Figure 3.15.

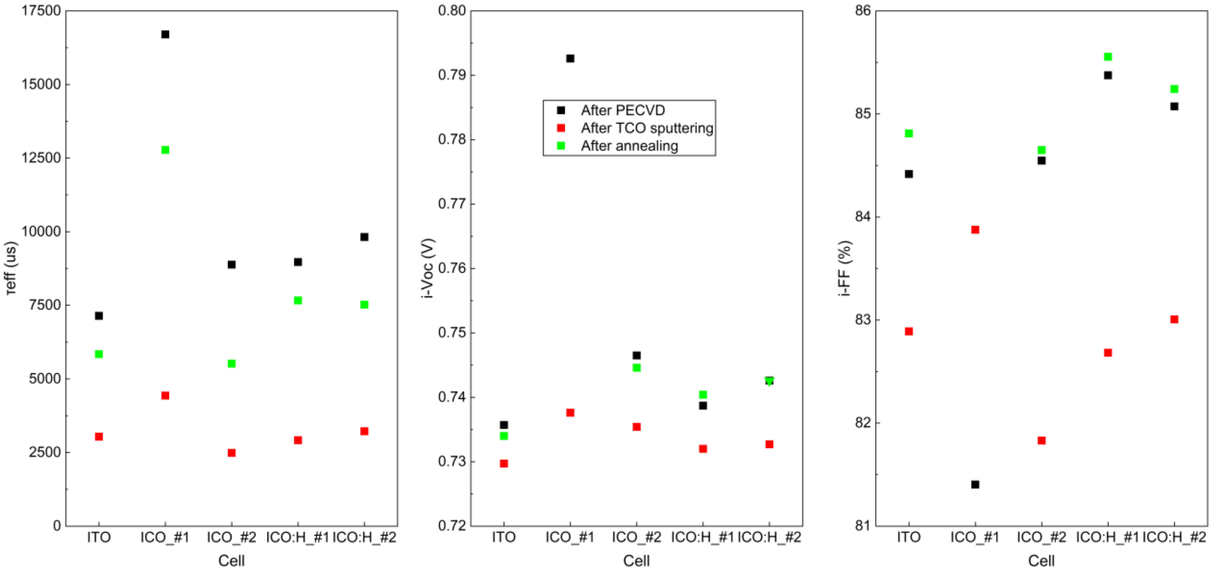

Figure 3.15 - Measurements of minority carrier lifetime (τ_{eff}), implied fill factor (i-FF), and implied open circuit voltage (i-V_{OC}) for the different fabricated cells.

After TCO sputtering, all the parameters were greatly reduced, for the sputtering process can significantly impact the surface of the underlying semiconductor layers[47]. Introducing stress, flaws, and damage to the passivation layers increases the probability of carrier recombination, leading to the reduced minority carrier lifetime observed, and, as a result, to the decreased V_{oc} and FF. When annealing is employed, some of the damage created by the TCO sputtering process is repaired. With better passivation quality, some of the mechanical stress produced during sputtering is relieved, and the surface recombination becomes lower, resulting in an increase in minority carrier lifetime. This leads to an increase in V_{oc} and FF, as observed in Figure 3.15. The lifetime and V_{oc} values were increased but not totally restored, and it is important to note that the annealing conditions, especially annealing temperature, are most likely suboptimal, but they were chosen based on device limitation. However, the FF values surpassed the initial values.

The ICO cell (#2) presented the highest i-V_{oc} of all the cells, reaching a value of 0.745 V, followed closely by the ICO:H cells, with an average value of 0.742 V. The reference ITO cell presented an i-V_{oc} value of 0.734 V. As for the i-FF, the best value was for the ICO:H cells, with an average value of 85.40%, followed by the ITO cell with 84.81% and, lastly, the ICO cell with 84.65%. The difference in the i-FF between the ICO and ICO:H cells can be due to the fact that the ICO:H layer presents a lower resistivity compared to the ICO layer ($7.28 \times 10^{-4}\ \Omega \cdot cm$ and $8.56 \times 10^{-4}\ \Omega \cdot cm$, respectively). This lower resistivity implies that the charge transport in this layer is more efficient, and this can improve the FF by lowering charge transport losses within the cell.

3.2.2 EQE

The external quantum efficiency (EQE) focuses on the efficiency of the solar cell in converting incident photons into electrical current that is collected externally from the device, taking into account reflection and transmission losses at interfaces. At a given wavelength, achieving a unity quantum efficiency requires the absorption of all photons of that wavelength, as well as the collection of all the resultant minority carriers. Figure 3.16 displays the EQE spectra for the best solar cells (ITO, ICO_#1 and ICO:H_#2) for each type of TCO, as well as the J_{sc} obtained from these measurements ($J_{sc,EQE}$).

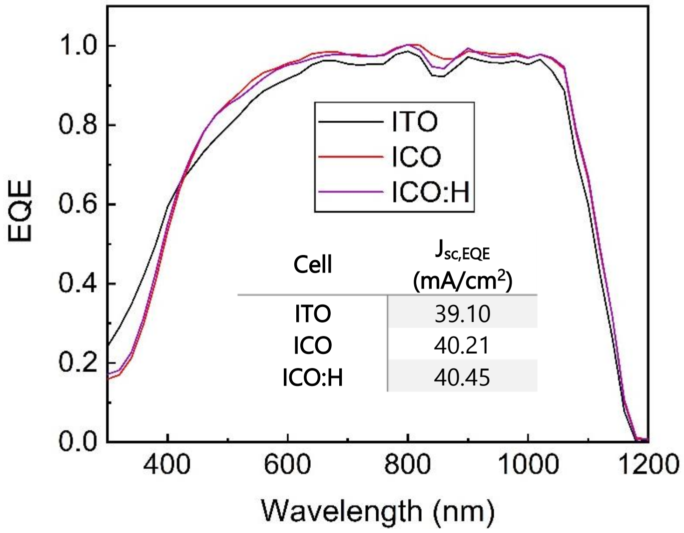

Cell	$J_{sc,EQE}$ (mA/cm^2)
ITO	39.10
ICO	40.21
ICO:H	40.45

Figure 3.16 - EQE measurements for the fabricated record cells, as well as for the ITO reference cell.

The EQE spectra presents some fluctuations from 600 nm to 1100 nm for all the cells. This could be due to some surface contamination or just to measurement errors[48].

In any case, the EQE results showed that using ICO/ICO:H enabled a current density enhancement of more than 1 mA/cm^2 when compared to the ITO reference cell. Although the

ITO cell presents a higher EQE for wavelengths below ~450 nm, the increased EQE of the ICO/ICO:H cell in the visible and near infrared region of the spectrum led to this increase in the current density from 39.10 mA/cm^2 (ITO) to 40.21 mA/cm^2 (ICO) and 40.45 mA/cm^2 (ICO:H).

3.2.3 JV Curves

The JV curves were utilized to obtain the solar cell parameters: V_{oc}, J_{sc}, FF and efficiency (Eff). The short-circuit current density (J_{sc}) represents the maximum photocurrent density attainable from the device when working under short-circuit conditions. It was obtained from the current values and the cell area (3.86 cm^2). Figure 3.17 shows these curves for the record cells, as well as the obtained cell parameters.

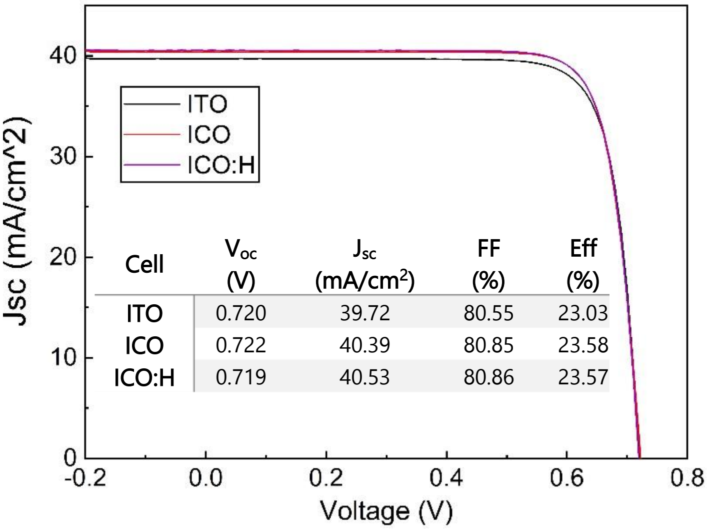

Cell	V_{oc} (V)	J_{sc} (mA/cm^2)	FF (%)	Eff (%)
ITO	0.720	39.72	80.55	23.03
ICO	0.722	40.39	80.85	23.58
ICO:H	0.719	40.53	80.86	23.57

Figure 3.17 - JV curves and cell parameters for the fabricated record cells, as well as for the ITO reference cell.

All the curves obtained showed similar behavior, with the biggest difference being the J_{sc}. The reference ITO cell presented a J_{sc} of 39.72 mA/cm^2. By applying ICO instead of ITO, this value increased to 40.39 mA/cm^2, and by using ICO:H, the J_{sc} increased even more to a value of 40.53 mA/cm^2. The measured J_{SC} in the I-V measurements was, as reported by others[23,49], slightly larger than the values obtained from the EQE curve.

The ICO:H cell presented the highest reduction when comparing its V_{oc} before and after the metallization process. From an i-V_{oc} of 0.743 V, we obtained a V_{oc} of 0.719 V (lowest value obtained among all the best cells), which is a drop of more than 20 mV. This shows that the quasi-Fermi level splitting of both majority and minority carriers within the absorber was not properly manifested in the external voltage[21,50,51].

Nevertheless, high efficiencies of 23.58% and 23.57% were achieved for the cell with ICO and ICO:H, respectively. When comparing these results to the cell fabricated with the reference ITO, a significant enhancement is obtained, since the efficiency for the ITO cell was 23.03%.

4

CONCLUSIONS AND FUTURE PERSPECTIVES

In this thesis, the impact of deposition parameters, such as oxygen flow, chamber pressure, sputtering power, and water vapor partial pressure, on the optoelectrical properties of 35-nm-thick cerium-doped In_2O_3 (ICO) films deposited by RF magnetron sputtering were studied. The effect of a post-deposition annealing process at 180 °C in an oven was also investigated. The obtained films exhibited enhanced mobilities and transparency when compared to the conventional standard indium tin oxide (ITO) films[22] at the PVMD group.

In the oxygen flow series, the carrier concentration was found to be decreased due to the gradual extinction of oxygen vacancies from the lattice. The best mobility obtained, considering the tradeoff between transmittance and conductivity, was of 29.4 cm^2/Vs for an oxygen flow of 5 sccm, and this value is already higher than that for the optimized ITO (28 cm^2/Vs) within the PVMD group. In the chamber pressure series, the carrier concentration suffered a decrease most likely due to contamination of the chamber with oxygen that could have come from the constant changing of the equipment's target. A pressure of $3 \times 10^{-3}\ mbar$ ensured the best tradeoff between the optoelectrical properties, presenting the lowest resistivity value of $1.4 \times 10^{-3}\ \Omega \cdot cm$ and a mobility of 41.13 cm^2/Vs. In the sputtering power series, the increased energy of the sputtered particles could have led to the formation of a denser film, indicating smaller crystal structures in the bulk, which translated to higher conductivity and carrier concentration but lower mobility. Considering the results for conductivity and optical transmittance, the final best mobility achieved for the ICO film was 44.22 cm^2/Vs, presenting an average transmittance of 85.23% and a resistivity of $8.56 \times 10^{-4}\ \Omega \cdot cm.$ For the hydrogenation series, the equipment could not reach the desired lower values of water vapor partial pressure, and the tested pressures were not steady throughout the entire deposition. Nevertheless, the addition of water vapor to the deposition had minimal impact in the mobility, increasing just to 44.56 cm^2/Vs. However, the carrier concentration increased in respect to the ICO film deposited with no water vapor, reaching a value of $1.92 \times 10^{20}/cm^3$. Transmittance/reflectance results showed that water vapor had minimal impact on the film's optical properties, but the conductivity increased in respect to the sample deposited with no water vapor in the chamber. Finally, the impact of a 5 min post-deposition annealing process at 180 °C in an oven was studied. The annealing temperature was set at that value due to device limitations. The carrier concentration decrease for all the annealing periods, and Tutsch, et al., (2021)[34] reported that this property in ICO:H films started to drop at temperatures around 130 °C. Annealing also generally degraded the transmittance for both ICO and ICO:H films. It has been reported elsewhere[40] that a 210 °C annealing process is the optimal temperature to anneal ICO films in air in order to achieve the best results. In contrast, annealing in vacuum has been shown[28] to reduce the resistivity due to the improved carrier concentration, leading to an increase in mobility from 51 cm^2/Vs to 71 cm^2/Vs. On device level, a nitrogen[34] annealing atmosphere has been reported to increase the J_{sc}.

Heating the substrate during deposition is known to help improve the crystallinity of ICO films and therefore reach higher mobilities in the range of 130-170 cm^2/Vs[27,31,32]. All the depositions performed in this thesis were performed at room temperature, so it would be interesting to study how this parameter would influence the properties of the film. Also, lower water vapor partial pressures, or even more controlled pressures during deposition, can also enhance the film's properties. Post-deposition annealing should also be studied for a 50-nm-thick layer for the conditions to be better adjusted for the final device. Moreover, since several important characterizations were not performed, such as crystallographic structure, chemical composition, surface's topography, etc., a lot of results could not be fully understood, so a better assessment for all the obtained results should be carried out to understand the effect of all these varied parameters.

At device level, high efficiencies of 23.58% and 23.57% were achieved for the cell with ICO and ICO:H, respectively, the first presenting a high V_{oc} of 0.722 V, and the latter a high J_{sc} of 40.53 mA/cm^2. When comparing these results to the cell fabricated with the reference ITO, a significant enhancement is obtained, placing ICO as remarkable substitute for ITO in the role of the TCO layer for various photovoltaic applications. Furthermore, a decoupled front/back choice of TCO (e.g. IWO front and ICO rear) might lead to further performance enhancement[23].

BIBLIOGRAPHY

1. Smets, A. H., Jäger, K., Isabella, O., Swaaij, R. A., and Zeman, M. *Solar Energy: The Physics and Engineering of Photovoltaic Conversion, Technologies and Systems*. (2016).

2. Home - Net Zero Climate. https://netzeroclimate.org/.

3. IEA – International Energy Agency. https://www.iea.org/.

4. Solar - IEA. https://www.iea.org/energy-system/renewables/solar-pv.

5. International Technology Roadmap for Photovoltaic (ITRPV) - vdma.org - VDMA. https://www.vdma.org/international-technology-roadmap-photovoltaic.

6. Blakers, A. Development of the PERC Solar Cell. *IEEE J. Photovoltaics* **9**, 629–635 (2019).

7. Feldmann, F., Bivour Reichel, M. C., Hermle, M. & Glunz, S. W. A PASSIVATED REAR CONTACT FOR HIGH-EFFICIENCY n-TYPE SILICON SOLAR CELLS ENABLING HIGH V OC S AND FF>82%. (2013).

8. DeWolf, S., Descoeudres, A., Holman, Z. C. & Ballif, C. High-efficiency silicon heterojunction solar cells: A review. *Green* **2**, 7–24 (2012).

9. Lin, H. *et al.* Silicon heterojunction solar cells with up to 26.81% efficiency achieved by electrically optimized nanocrystalline-silicon hole contact layers. *Nat. Energy 2023 88* **8**, 789–799 (2023).

10. Tanaka, M. *et al.* Development of new a-si/c-si heterojunction solar cells: Acj-hit (artificially constructed junction- heterojunction with intrinsic thin-layer). *Jpn. J. Appl. Phys.* **31**, 3518–3522 (1992).

11. Zhao, Y. *et al.* Effects of (i)a-Si:H deposition temperature on high-efficiency silicon heterojunction solar cells. *Prog. Photovoltaics Res. Appl.* (2022) doi:10.1002/PIP.3620.

12. Sai, H. *et al.* Impact of intrinsic amorphous silicon bilayers in silicon heterojunction solar cells. *J. Appl. Phys.* **124**, (2018).

13. Procel, P. ;, Yang, G. ;, Isabella, O. ; & Zeman, M. Theoretical evaluation of contact stack for high efficiency IBC-SHJ solar cells. *Sol. Energy Mater. Sol. Cells Cit.* (2018) doi:10.1016/j.solmat.2018.06.021.

14. Xu, Y. *et al.* Heterojunction solar cells with n-type nanocrystalline silicon emitters on p-type c-Si wafers. *J. Non. Cryst. Solids* **352**, 1972–1975 (2006).

15. Seif, J. P. *et al.* Strategies for Doped Nanocrystalline Silicon Integration in Silicon Heterojunction Solar Cells. *IEEE J. Photovoltaics* **6**, 1132–1140 (2016).

16. Nogay, G. *et al.* Nanocrystalline Silicon Carrier Collectors for Silicon Heterojunction Solar Cells and Impact on Low-Temperature Device Characteristics. *IEEE J. Photovoltaics* **6**, 1654–1662 (2016).

17. Mazzarella, L. *et al.* Nanocrystalline n-type silicon oxide front contacts for silicon heterojunction solar cells: Photocurrent enhancement on planar and textured substrates. *IEEE J. Photovoltaics* **8**, 70–78 (2018).

18. Zhao, Y. *et al.* Doped hydrogenated nanocrystalline silicon oxide layers for high-efficiency c-Si heterojunction solar cells. *Prog. Photovoltaics Res. Appl.* **28**, 425–435 (2020).

19. Procel, P. *et al.* The role of heterointerfaces and subgap energy states on transport mechanisms in silicon heterojunction solar cells. *Prog. Photovoltaics Res. Appl.* **28**, 935–945 (2020).

20. Limodio, G. *et al.* Copper-Plating Metallization with Alternative Seed Layers for c-Si Solar Cells Embedding Carrier-Selective Passivating Contacts. *IEEE J. Photovoltaics* **10**, 372–382 (2020).

21. Han, C. *et al.* Controllable Simultaneous Bifacial Cu-Plating for High-Efficiency Crystalline Silicon Solar Cells. *Sol. RRL* **6**, 1–10 (2022).

22. Han, C. *et al.* High-Mobility Hydrogenated Fluorine-Doped Indium Oxide Film for Passivating Contacts c-Si Solar Cells. *ACS Appl. Mater. Interfaces* **11**, 45586–45595 (2019).

23. Han, C. *et al.* Room-temperature sputtered tungsten-doped indium oxide for improved current in silicon heterojunction solar cells. *Sol. Energy Mater. Sol. Cells* **227**, 111082 (2021).

24. Aissa, B., Zakaria, Y., Shetty, A. R., Samara, A. & Broussillou, C. High Electron-Mobility of a Transparent and Conductive Zr-Doped In2O3Deposited by Reactive Magnetron Sputtering. *Conf. Rec. IEEE Photovolt. Spec. Conf.* 71–73 (2021) doi:10.1109/PVSC43889.2021.9518643.

25. Wibowo, A. S. B. Hydrogenated Indium Oxide (IO:H) for Thin Film Solar Cell. 82 (2016).

26. Balestrieri, M. Transparent conductive oxides with photon converting properties in view of photovoltaic applications : the cases of rare earth-doped zinc oxide and cerium oxide HAL Id : tel-01132180. (2018).

27. Kobayashi, E., Watabe, Y. & Yamamoto, T. High-mobility transparent conductive thin films of cerium-doped hydrogenated indium oxide. *Appl. Phys. Express* **8**, (2015).

28. Dey, K., Aberle, A. G., van Eek, S. & Venkataraj, S. Superior optoelectrical properties of magnetron sputter-deposited cerium-doped indium oxide thin films for solar cell applications. *Ceram. Int.* **47**, 1798–1806 (2021).

29. An, S. *et al.* Cerium-doped indium oxide transparent electrode for semi-transparent perovskite and perovskite/silicon tandem solar cells. *Sol. Energy* **196**, 409–418 (2020).

30. Fortunato, E., Ginley, D., Hosono, H. & Paine, D. C. Transparent conducting oxides for photovoltaics. *MRS Bull.* **32**, 242–247 (2007).

31. Chen, Q. & China SC. Reactive Plasma Deposition of TCOs. in *SiliconPV Conference: 13th International Conference on Crystalline Silicon Photovoltaics* (2023).

32. Kobayashi, E., Watabe, Y., Yamamoto, T. & Yamada, Y. Cerium oxide and hydrogen co-doped indium oxide films for high-efficiency silicon heterojunction solar cells. *Sol. Energy Mater. Sol. Cells* **149**, 75–80 (2016).

33. Haacke, G. New figure of merit for transparent conductors. *J. Appl. Phys.* **47**, 4086 (2008).

34. Tutsch, L. *et al.* The sputter deposition of broadband transparent and highly conductive cerium and hydrogen co-doped indium oxide and its transfer to silicon heterojunction solar cells. *Prog. Photovoltaics Res. Appl.* **29**, 835–845 (2021).

35. Erfurt, D. *et al.* Improved electrical properties of pulsed DC magnetron sputtered hydrogen doped indium oxide after annealing in air. *Mater. Sci. Semicond. Process.* **89**, 170–175 (2019).

36. Choi, C. G. *et al.* Effects of oxygen partial pressure on the microstructure and electrical properties of indium tin oxide film prepared by d.c. magnetron sputtering. *Thin Solid Films* **258**, 274–278 (1995).

37. Avino, F. *et al.* Improved film density for coatings at grazing angle of incidence in high power impulse magnetron sputtering with positive pulse. *Thin Solid Films* **706**, 138058 (2020).

38. Tchenka, A. *et al.* Effect of RF Sputtering Power and Deposition Time on Optical and Electrical Properties of Indium Tin Oxide Thin Film. *Adv. Mater. Sci. Eng.* **2021**, (2021).

39. Lee, J. H., Kim, Y. H., Ahn, S. J., Ha, T. H. & Kim, H. S. Grain-size effect on the electrical properties of nanocrystalline indium tin oxide thin films. *Mater. Sci. Eng. B* **199**, 37–41 (2015).

40. Liu, H. *et al.* Effect of annealing treatment on properties of Ce-doped indium oxide (ICO) transparent conductive oxide films. *J. Mater. Sci. Mater. Electron.* **34**, 1–7 (2023).

41. Garcia, C. B., Ariza, E. & Tavares, C. J. Influence of substrate temperature and post-annealing treatment on the microstructure and electric properties of ZnO:Al thin films deposited by sputtering. *Mater. Sci. Forum* **730–732**, 215–220 (2013).

42. Ahmed, N. M. *et al.* The effect of post annealing temperature on grain size of indium-tin-oxide for optical and electrical properties improvement. *Results Phys.* **13**, 102159 (2019).

43. Luderer, C., Messmer, C., Hermle, M. & Bivour, M. Transport Losses at the TCO/a-Si:H/c-Si Heterojunction: Influence of Different Layers and Annealing. *IEEE J. Photovoltaics* **10**, 952–958 (2020).

44. Haschke, J. *et al.* Annealing of Silicon Heterojunction Solar Cells: Interplay of Solar Cell and Indium Tin Oxide Properties. *IEEE J. Photovoltaics* **9**, 1202–1207 (2019).

45. Yu, J. *et al.* Copper metallization of electrodes for silicon heterojunction solar cells: Process, reliability and challenges. *Sol. Energy Mater. Sol. Cells* **224**, 110993 (2021).

46. Zhang, D. *Surface passivation and optical design of silicon heterojunction solar cells*. (2015).

47. Feldmann, F. *et al.* Carrier-selective contacts for Si solar cells. *Appl. Phys. Lett.* **104**, (2014).

48. Kanda, H. *et al.* Al2O3/TiO2 double layer anti-reflection coating film for crystalline silicon solar cells formed by spray pyrolysis. *Energy Sci. Eng.* **4**, 269–276 (2016).

49. Li, H. *et al.* Influence of Room Temperature Sputtered Al-Doped Zinc Oxide on Passivation Quality in Silicon Heterojunction Solar Cells. *IEEE J. Photovoltaics* **9**, 1485–1491 (2019).

50. Grubel, B. *et al.* Direct contact electroplating sequence without initial seed layer for bifacial TOPCon solar cell metallization. *IEEE J. Photovoltaics* **11**, 584–590 (2021).

51. Bivour, M., Reusch, M., Feldmann, F., Hermle, M. & Glunz, S. Requirements for Carrier Selective Silicon Heterojunctions. *Proc. 24th Work. Cryst. Silicon Sol. Cells Modul.* 1–9 (2014).

A

RF SPUTTERED ICO

A.1 Uniformity Measurements

To check thickness and sheet resistance uniformity, measurements were performed in different parts of the samples, as shown in Figure A.1, respectively.

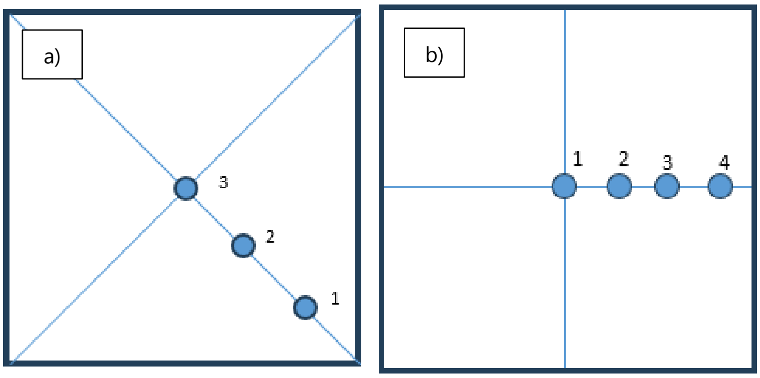

Figure A.1 - Points were a) thickness and b) sheet resistance were measured to check for the uniformity of the films.

A.2 Sheet Resistance Measurements

In this section, the plots for sheet resistance measurements, as well as its error bars, are displayed for the different optimization series.

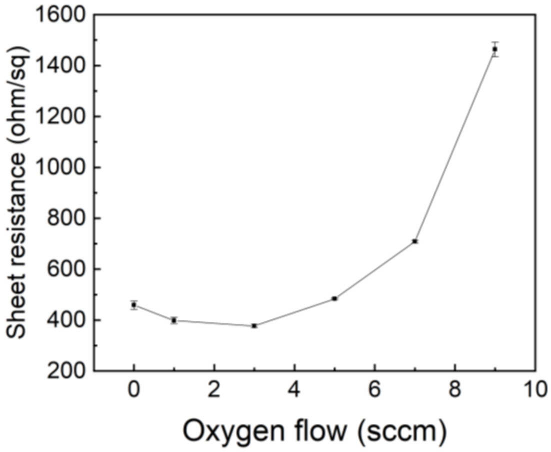

Figure A.2 - Sheet resistance measurements and the corresponding error bar for the oxygen flow series.

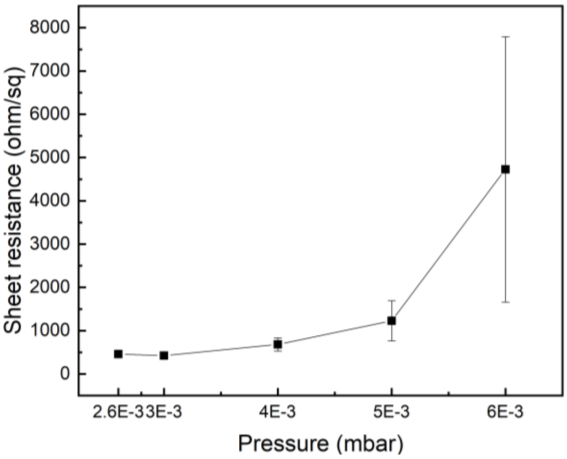

Figure A.3 - Sheet resistance measurements and the corresponding error bar for the chamber pressure series.

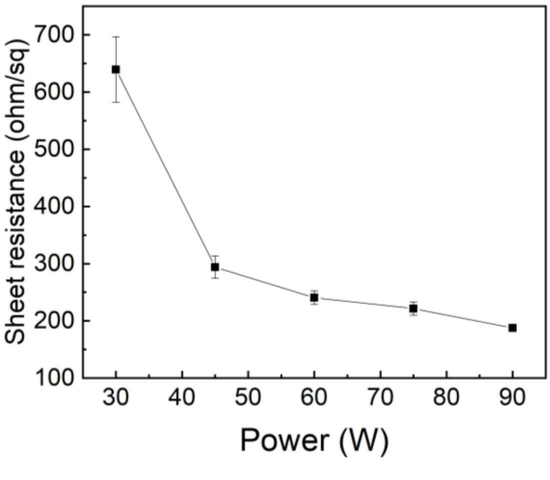

Figure A.4 - Sheet resistance measurements and the corresponding error bar for the sputtering power series.

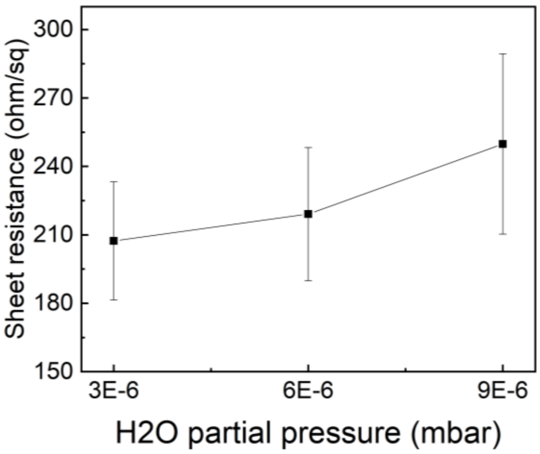

Figure A.5 - Sheet resistance measurements and the corresponding error bar for the hydrogenation series.

2023

MARIA M. R. MAGALHÃES

OPTIMIZATION OF RF MAGNETRON SPUTTERING OF CERIUM-DOPED INDIUM OXIDE FOR SILICON HETEROJUNCTION SOLAR CELLS

NOVA SCHOOL OF
SCIENCE & TECHNOLOGY